


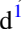






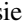
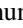
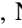

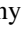
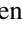
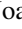








Brightest Cluster Galaxy Formation in the $z = 4.3$ Protocluster SPT 2349-56: Discovery of a Radio-loud Active Galactic Nucleus

Scott C. Chapman^{1,2,3,4} , Ryley Hill³, Manuel Aravena⁵ , Melanie Archipley^{6,7} , Arif Babul⁸, James Burgoyne³, Rebecca E. A. Canning⁹, Roger P. Deane^{10,11}, Carlos De Breuck¹², Anthony H. Gonzalez¹³ , Christopher C. Hayward¹⁴ , Seon Woo Kim⁶, Matt Malkan¹⁵ , Dan P. Marrone¹⁶ , Vincent McIntyre¹⁷, Eric Murphy¹⁸ , Emily Pass^{1,19} , Ryan W. Perry¹, Kedar A. Phadke^{6,7} , Douglas Rennehan¹⁴, Cassie Reuter⁶ , Kaja M. Rotermond²⁰ , Douglas Scott³ , Nick Seymour¹⁷, Manuel Solimano⁵ , Justin Spilker²¹ , Anthony A. Stark¹⁹ , Nikolaus Sulzenauer²² , Nick Tothill²³ , Joaquin D. Vieira^{6,7} , David Vizgan⁶ , George Wang³, and Axel Weiss²² 

¹ Department of Physics and Atmospheric Science, Dalhousie University, Halifax, NS, B3H 4R2, Canada; scott.chapman@dal.ca

² NRC Herzberg Astronomy and Astrophysics, 5071 West Saanich Road, Victoria, BC, V9E 2E7, Canada

³ Department of Physics and Astronomy, University of British Columbia, Vancouver, BC, V6T 1Z1, Canada

⁴ Eureka Scientific Inc, Oakland, CA 94602, USA

⁵ Núcleo de Astronomía, Facultad de Ingeniería y Ciencias, Universidad Diego Portales, Av. Ejército 441, Santiago, Chile

⁶ Department of Astronomy, University of Illinois, 1002 West Green Street, Urbana, IL 61801, USA

⁷ Center for Astrophysical Surveys, National Center for Supercomputing Applications, 1205 West Clark Street, Urbana, IL 61801, USA

⁸ Department of Physics and Astronomy, University of Victoria, Victoria, BC, V8P 1A1, Canada

⁹ Institute of Cosmology and Gravitation, University of Portsmouth, Dennis Sciamia Building, Portsmouth, PO1 3FX, UK

¹⁰ Wits Centre for Astrophysics, School of Physics, University of the Witwatersrand, 1 Jan Smuts Avenue, Johannesburg, 2000, South Africa

¹¹ Department of Physics, University of Pretoria, Private Bag X20, Pretoria 0028, South Africa

¹² European Southern Observatory, Karl Schwarzschild Strasse 2, D-85748 Garching, Germany

¹³ Department of Astronomy, University of Florida, 211 Bryant Space Science Center, Gainesville, FL 32611-2055, USA

¹⁴ Center for Computational Astrophysics, Flatiron Institute, 162 Fifth Avenue, New York, NY 10010, USA

¹⁵ Department of Physics and Astronomy, University of California, Los Angeles, CA 90095, USA

¹⁶ Steward Observatory, University of Arizona, 933 North Cherry Avenue, Tucson, AZ 85721, USA

¹⁷ International Center for Radio Astronomy Research, Curtin University, GPO Box U1987, Perth, WA 6845, Australia

¹⁸ NRAO National Radio Astronomy Observatory, 520 Edgemont Road, Charlottesville, VA 22903, USA

¹⁹ Harvard-Smithsonian Center for Astrophysics, 60 Garden Street, Cambridge, MA 02138, USA

²⁰ Lawrence Berkeley National Laboratory, Berkeley, CA 94720, USA

²¹ Department of Physics and Astronomy and George P. and Cynthia Woods Mitchell Institute for Fundamental Physics and Astronomy, Texas A&M University, 4242 TAMU, College Station, TX 77843-4242, USA

²² Max-Planck-Institut für Radioastronomie, Auf dem Hugel 69, Bonn, D-53121, Germany

²³ School of Science, Western Sydney University, Locked Bag 1797, Penrith, NSW 2751, Australia

Received 2022 December 16; revised 2023 October 13; accepted 2023 November 1; published 2024 January 18

Abstract


We have observed the $z = 4.3$ protocluster SPT2349–56 with the Australia Telescope Compact Array (ATCA) with the aim of detecting radio-loud active galactic nuclei (AGNs) among the ~ 30 submillimeter (submm) galaxies (SMGs) identified in the structure. We detect the central complex of submm sources at 2.2 GHz with a luminosity of $L_{2.2} = (4.42 \pm 0.56) \times 10^{25} \text{ W Hz}^{-1}$. MeerKAT and the Australian Square Kilometre Array Pathfinder also detect the source at 816 MHz and 888 MHz, respectively, constraining the radio spectral index to $\alpha = -1.45 \pm 0.16$, implying $L_{1.4,\text{rest}} = (2.2 \pm 0.2) \times 10^{26} \text{ W Hz}^{-1}$. The radio observations do not have sufficient spatial resolution to uniquely identify one of the three Atacama Large Millimeter/submillimeter Array (ALMA) galaxies as the AGN, however the ALMA source properties themselves suggest a likely host. This radio luminosity is $\sim 100\times$ higher than expected from star formation, assuming the usual far-infrared–radio correlation, indicating an AGN driven by a forming brightest cluster galaxy. None of the SMGs in SPT2349–56 show signs of AGNs in any other diagnostics available to us, highlighting the radio continuum as a powerful probe of obscured AGNs. We compare these results to field samples of radio sources and SMGs, along with the 22 gravitationally lensed SPT-SMGs also observed in the ATCA program, as well as powerful radio galaxies at high redshifts. The $(3.3 \pm 0.7) \times 10^{38} \text{ W}$ of power from the radio-loud AGN sustained over 100 Myr is comparable to the binding energy of the gas mass of the central halo, and similar to the instantaneous energy injection from supernova feedback from the SMGs in the core region. The SPT2349–56 radio-loud AGNs may be providing strong feedback on a nascent intracluster medium.

Unified Astronomy Thesaurus concepts: [Galaxy clusters \(584\)](#)

1. Introduction

Submillimeter (submm) galaxies (SMGs) are important sites of stellar mass buildup at cosmic noon and earlier (e.g.,

Chapman et al. 2003, 2005; Smail et al. 2004), with star formation rates (SFRs) as high as hundreds to thousands of solar masses per year. Several studies have also suggested that SMGs may be good tracers of dark matter halos at early cosmic time (e.g., Blain et al. 2004; Chen et al. 2016; Dudzevičiūtė et al. 2020). Simulations conducted by Miller et al. (2015) found that, while many dark matter halos at $z = 2-4$ do not contain any SMGs, large and rare associations of five or more

 Original content from this work may be used under the terms of the [Creative Commons Attribution 4.0 licence](#). Any further distribution of this work must maintain attribution to the author(s) and the title of the work, journal citation and DOI.

SMGs do trace massive overdensities of dark matter that have the potential of evolving into present-day massive clusters. Supporting this, in the recent past several high-redshift protoclusters have been identified entirely through their submm emission (e.g., Chapman et al. 2009; Casey et al. 2015; Miller et al. 2018; Oteo et al. 2018; Gómez-Guijarro et al. 2019; Wang et al. 2021). Other protoclusters discovered through optical surveys were subsequently found to have large submm source overdensities (e.g., Daddi et al. 2009; Dannerbauer et al. 2014; Lacaille et al. 2019).

Active galactic nuclei (AGNs) and star formation processes in galaxy evolution are clearly related (e.g., Kormendy & Ho 2013). Enhanced AGN activity relative to the field environment has been found in massive protoclusters at $z=2-3$ (e.g., Pentericci et al. 2002; Lehmer et al. 2009; Digby-North et al. 2010), which is likely related to the enhancement of star formation in galaxy protocluster members (e.g., Elbaz et al. 2007; Chapman et al. 2009; Brodwin et al. 2013; Casey et al. 2015; Gilli et al. 2019). The suppression of star formation in galaxy clusters requires mechanical and radiative feedback, which is naturally generated by AGNs. Extended X-ray emission has been detected in clusters, showing empty regions or cavities in the hot gas (e.g., Fabian 2012), which can naturally be explained as shocked gas from the feedback. The Clusters Around Radio-Loud AGN survey of around 400 high-redshift radio galaxies (HzRGs) from $z=1-3$ (Wylezalek et al. 2013) showed that in the majority of cases the radio AGN is located near the center of the galaxy overdensity as traced by their stellar mass (Spitzer/IRAC emission). This is strong evidence that radio galaxy feedback in a growing brightest cluster galaxy (BCG) is important for the evolution of massive galaxy clusters.

Galaxy overdensities in the high-redshift Universe have likely not yet virialized (e.g., Chiang et al. 2013; Overzier et al. 2013; Muldrew et al. 2015). They have abundant reservoirs of cold gas to supply star formation, while the ongoing mergers between galaxies expected in the dense environments provide triggers for star formation. Mergers can also provide the tidal torques necessary for the gas to overcome its angular momentum and fall to the accretion disk of the supermassive black hole (SMBH). AGNs require this nuclear accretion as a power source. This is in contrast to low redshifts, where structures are virialized, and both AGNs and star formation are largely suppressed in cluster galaxies (Kauffmann et al. 2004; Martini et al. 2006; van Breukelen et al. 2009; Rasmussen et al. 2012; Ehlert et al. 2014). Studies of AGNs in protoclusters have recently become a viable endeavor, with relatively deep Chandra and XMM-Newton observations at $z=1.5-3$ (e.g., Lehmer et al. 2009; Wang et al. 2013; Travascio et al. 2020; Tozzi et al. 2022a, 2022b). Continuing to study the rich variety of protoclusters and extending these studies to earlier times can inform how host galaxies are affected by their SMBHs, as well as the connection to the surrounding environment. In the $z=3.09$ SSA22 protocluster, 50% of the SMGs were found to host X-ray-luminous AGNs (Umehata et al. 2019)—a clear excess over the 15% found for field SMGs (e.g., Wang et al. 2013). At larger distances, an overdensity of 10 SMGs found by the Herschel Space Telescope at $z=4.0$ (Oteo et al. 2018) has been studied by Chandra in the X-ray (Vito et al. 2020) and in the radio (Oteo et al. 2018), revealing no significant excess of AGN activity in the system over field SMGs (22% versus 15%, respectively).

The 2500 deg² survey conducted by the South Pole Telescope (SPT; Vieira et al. 2010; Everett et al. 2020) at 3.0 mm, 2.0 mm, and 1.4 mm has uncovered a small population of nine millimeter sources ranging from $z=3-7$, which are extremely luminous yet apparently not gravitationally lensed (e.g., Spilker et al. 2016; Reuter et al. 2020; Wang et al. 2021). A well-characterized example of this is SPT2349–56, a protocluster system at $z=4.303$ (Miller et al. 2018). Observations at 870 μm using the Large APEX BOlometer CAmera (LABOCA; Siringo et al. 2009) on the Atacama Pathfinder Experiment (APEX; Güsten et al. 2006) telescope (with a 19" beam size) first revealed an extended structure with two distinct lobes connected by a bridge with a combined flux density of $S_{870\mu\text{m}} = (106 \pm 8)$ mJy (Miller et al. 2018; Wang et al. 2021). Follow-up observations with the Atacama Large Millimeter-submillimeter Array (ALMA; Wootten & Thompson 2009) measured the redshift of its brightest central source through ¹²CO lines (Strandet et al. 2016), and then resolved the structure into over 30 submm-luminous sources (Miller et al. 2018; Hill et al. 2020; Rotermund et al. 2021), with a velocity dispersion suggesting a central halo mass of around $10^{13} M_{\odot}$. The faintest of these submm sources at $S_{870\mu\text{m}} < 1$ mJy would not be detectable with single-dish facilities due to confusion. A Very Large Telescope (VLT)/MUSE observation revealed the presence of a Ly α blob (LAB), with a linear size of about 60 kpc, close to the core of SPT2349–56 (Apostolovski et al. 2023). None of the other protocluster SMGs were detected as Ly α emitters in the MUSE data. Ly α halos are commonplace in most HzRG protoclusters (Venemans et al. 2007). Similar objects are often found in protoclusters identified through other means, for example optical galaxy overdensities (Overzier 2016), and indicate the presence of significant amounts of neutral gas in the assembling cluster.

This paper presents a search for radio detections of members of the SPT2349–56 cluster. Section 2 describes the radio and (sub)millimeter observations. Section 3 presents the results derived from the source extraction and analysis. In Section 4, we discuss the detected central radio source, the energy injected into a growing intracluster medium (ICM), and the implications for radio-loud AGNs in protoclusters. We conclude in Section 5. Throughout our analysis, a Hubble constant of $H_0 = 70 \text{ km s}^{-1} \text{ Mpc}^{-1}$ and density parameters of $\Omega_{\Lambda} = 0.7$ and $\Omega_{\text{m}} = 0.3$ are assumed, resulting in a proper angular scale of 6.88 kpc arcsec⁻¹ at $z=4.3$.

2. Data

2.1. ATCA Observations

SPT2349–56 was observed by the Australia Telescope Compact Array (ATCA) at 2.2, 5.5, and 9.0 GHz between 2012 January 23 and 27, as part of a program (C1563) to observe 23 SPT-SMGs (described in Appendix C). We used the Compact Array Broadband Backend configured in the 1M-0.5k mode, which leads to a bandwidth of 2 GHz per correlator window with 1 MHz per channel of spectral resolution. The observations were performed in the most extended ATCA configuration, 6A, with six working 22 m antennas. The on-source time was 34 minutes, which was typical for all SPT-SMGs observed (see Table 5 in Appendix C). The data were edited, calibrated, and imaged using the Miriad package. Data affected by known radio frequency interference (RFI) or with bad visibility ranges were flagged accordingly. We estimate an absolute

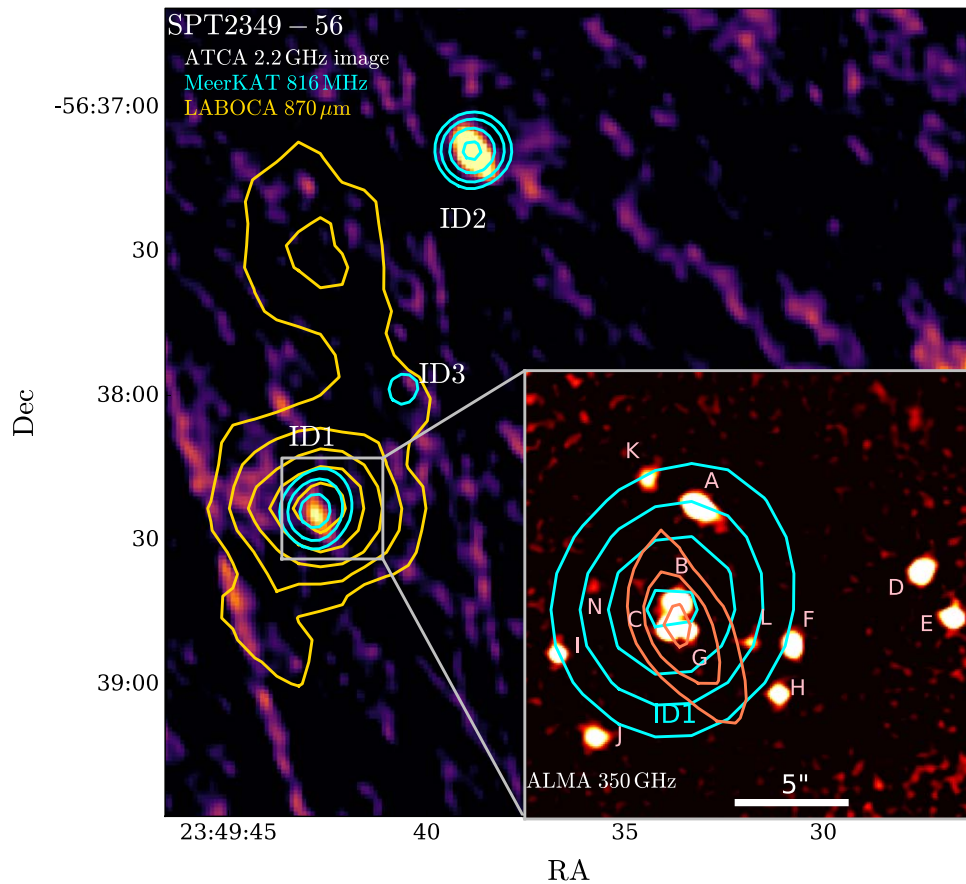


Figure 1. Background: ATCA 2.2 GHz imaging of the SPT2349–56 region, with gold contours highlighting the 110 mJy extended LABOCA source at 870 μm (Miller et al. 2018). An ATCA radio source (ID1) is identified near the LABOCA core, with a MeerKAT 816 MHz source (cyan contours) overlapping (ASKAP also detects an ID1 at $\sim 5\sigma$). MeerKAT also detects an ID3 radio source within the LABOCA structure, identified to a foreground $z = 0.66$ SMG. The bright ATCA +MeerKAT source to the northwest is identified with a Milky Way star (ID2 in Table 1). The linear ATCA feature east of SPT2349–56 is from the synthesized beam structure of a bright 20 mJy source to the south (see Appendix A). Inset: a $20'' \times 20''$ zoom in of ALMA 350 GHz continuum imaging (Hill et al. 2020) with overlays of ATCA 2.2 GHz (coral) and MeerKAT 816 MHz (cyan). ATCA contours start at 3.7σ revealing the FWHM of the source ($4'' \times 8''$). MeerKAT contours start at 5σ , and the FWHM of the source is $10''$ diameter. ALMA sources are named from Miller et al. (2018) in order of their 850 μm flux density. The radio detection of the B-C-G complex of galaxies is evident.

calibration uncertainty of 5% at 2.2 and 5.5 GHz, and 10% at 9.0 GHz. We inverted the visibilities using natural weighting, leading to beam sizes of $7''.7 \times 4''.2$, $3''.2 \times 2''.1$, and $2''.0 \times 1''.3$ at 2.2, 5.5, and 9.0 GHz, respectively, with associated rms noise values of 27, 40, and 53 $\mu\text{Jy beam}^{-1}$, respectively. Figure 1 displays the ATCA 2.2 GHz map surrounding SPT2349–56, revealing a well-detected (8σ) source near the core of SPT2349–56. No sources at 5.5 or 9.0 GHz are found in the vicinity of SPT2349–56. The ATCA sources surrounding SPT2349–56 out to 1 Mpc in projection are listed in Table 1, and the wider-field ATCA map is shown in Appendix A.

The shortest baseline is 30 m and the images should be sensitive to emission on angular scales up to a few arcminutes. In principle, these data should not be missing any flux on the scales covering both the ATCA and MeerKAT/ASKAP (see below) sources, although the ATCA data will be less sensitive to lower-surface-brightness emission. However, the short 34 minutes integration, with quite limited signal-to-noise ratio (S/N), may still be missing some structure due to sparse uv coverage. Similar issues were discussed in an ATCA snapshot survey of distant HzRGs (De Breuck et al. 2000) and are elaborated in Section 4.

Table 1
Radio-selected Sources within a Radius of 1 Mpc in Projection ($140''$) of SPT2349–56

ID	R.A.	Decl.	Freq. (GHz)	Flux (μJy)
ID1	8.98	$<159^c$
ID1	5.47	$<120^c$
ID1	23:49:42.760	-56:38:25.05	2.17	214 ± 27
ID1 ^a	23:49:42.55	-56:38:19.4	0.888	867 ± 189
ID1 ^b	23:49:42.76	-56:38:24.4	0.816	778 ± 12
ID2	23:49:38.838	-56:37:09.63	2.17	547 ± 36
ID2 ^a	23:49:38.750	-56:37:06.09	0.888	1324 ± 182
ID3 ^b	23:49:40.551	-56:37:58.47	0.816	211 ± 12

Notes.

^a ASKAP measurement.

^b MeerKAT measurement.

^c 3σ ATCA limit.

2.2. MeerKAT Observations

Observations with the MeerKAT radio telescope (Jonas & MeerKAT Team 2016) were carried out on SPT 2349–56 in the UHF band over three epochs during a set of test observations for the 50 deg² MeerKAT South Pole Telescope Survey. The

first phase of this survey will reach a continuum depth of $\sim 10 \mu\text{Jy beam}^{-1}$ with an angular resolution of $\sim 8''$, which is highly dependent on the imaging weights selected. The *UHF* band covers a usable range of 580–1015 MHz, and the 544 MHz of digitized bandwidth is split into 32,768 channels, each 16.6 kHz wide and with a correlator dump time of 8 s. The three epochs were carried out on 2022 November 15 and 16, and 2023 January 4. Each epoch was 72 minutes in duration (53 minutes on-source) and scheduled to explore *UHF* imaging performance for a typical SPT field for this observation duration over a range of three different starting hour angles. The three scans are nearly identical, with a total of 59, 61, and 59 antennas participating in each, respectively. Each epoch consisted of a single pointing centered on the target at $(\alpha, \delta) = 23^{\text{h}}49^{\text{m}}42^{\text{s}}.5, -56^{\text{d}}38^{\text{m}}22^{\text{s}}.5$. The absolute flux and bandpass calibrator, J0408–6545 was used. Time-varying complex gains were solved for, using interleaved observations of the gain calibrator J2329–4730, with an approximate scan length of 2 minutes every 28 minutes. Two 5 minutes scans were carried out on the flux and bandpass calibrator at the start and end of each epoch.

The data were reduced using OXKAT,²⁴ a semiautomated MeerKAT data-analysis pipeline fully described in Heywood (2020) and Heywood et al. (2022). Briefly, the calibration strategy begins with cross-calibration, which includes averaging down to a channel width of 0.53 MHz, manual flagging of bad data and automated flagging of known and low-level RFI using the TRICOLOR software package.²⁵ Absolute flux calibration assumes J0408–6545 is a point source with a Stokes *I* flux density of $S_\nu = 17.066 \text{ Jy beam}^{-1}$ with a spectral index of $\alpha = -1.179$ (where $S \propto \nu^\alpha$) at a reference frequency of 1284 MHz. Bandpass calibration also uses J0408–6545 as a reference source, while time-variable complex gains are solved for using J2329–4730 in eight spectral bins and a solution interval of 2 minutes. The solutions are then all transferred to the target visibilities. Apart from flagging, the cross-calibration process uses standard CASA tasks (McMullin et al. 2007) and is iterative, with each round included flagging to improve RFI excision and the resultant calibration and image quality.

For self-calibration, an initial deconvolution mask of the target field is created using a shallow unmasked clean down to $50 \mu\text{Jy beam}^{-1}$ with a Briggs’ ROBUST weighting of -0.5 . This mask is then used to create an initial sky model, which is iteratively improved along with the time-variable complex gain solutions through two rounds of antenna-based delay self-calibration using the CUBICAL package (Kenyon et al. 2018), splitting the data into eight spectral bins and time intervals of 1 minute. Multifrequency synthesis imaging is performed with WSCLEAN (Offringa et al. 2014) and includes data from all three epochs (159 minutes on-source in total). The final image rms of the antenna-based (i.e., direction-independent) self-calibrated map is $\sigma \sim 5 \mu\text{Jy beam}^{-1}$ (ROBUST = 0) toward the outskirts of the image beyond the primary beam’s main lobe, which has a FWHM of $\sim 1.6 \text{ deg}$ at 816 MHz. We do not perform any direction-dependent calibration as the region of interest in this paper has a Gaussian-like noise distribution. As a final step, a $13,400 \times 13,400$ pixel image (pixel size = $1''.3$, image area $4.8 \times 4.8 \text{ deg}^2$) with a Briggs’ ROBUST weighting of -1.5 is generated to maximize the image sensitivity. This

Table 2
ALMA Observing Programs Used for Follow-up Analysis

ID	Date	Freq. (GHz)	σ_{ctm} (μJy)	Beam ($''$)	Array
2015.1.01543.T	03/20/16	148.3	10	0.88	C36-2/3
2018.1.00058.S	10/03/18	146.8	12	0.28	C43-6
2021.1.01313.S	07/27/22	146.3	21	0.27	C-6
2021.1.01313.S	09/01/22	231.9	31	0.47	C-4

Note. Details on additional ALMA Band 7 observations used in this paper can be found in Hill et al. (2020). Here the frequency is the central frequency between the upper and lower sidebands, the continuum sensitivity is calculated at the center of the primary beam and averaged over the upper and lower sidebands, and the beam is the average circular synthesized beam FWHM.

results in a point-spread function FWHM of $9''.3$ by $9''.2$, at a position angle (PA) of 59.4 deg east of north. The rms sensitivity in the vicinity of the target source of this final map is $\sigma = 12 \mu\text{Jy beam}^{-1}$ and the effective frequency is 816 MHz.

2.3. ASKAP Observations

The Australian Square Kilometre Array Pathfinder (ASKAP) comprises 36 12 m dishes located in the Inyarrimanha Ilgari Bundra²⁶ at the CSIRO Murchison Radio-astronomy Observatory in Western Australia, observing between 700 MHz and 1.8 GHz, with an instantaneous bandwidth of up to 288 MHz. ASKAP is equipped with phased-array feeds (Hotan et al. 2014; McConnell et al. 2016), capable of simultaneously forming up to 36 independent beams, covering some 30 deg^2 .

SPT2349–56, along with all 22 of the lensed SPT-SMGs in the ATCA program, were observed by the Rapid ASKAP Continuum Survey (RACS; McConnell et al. 2020), covering the sky south of $+41 \text{ deg}$ decl. at a central frequency of 887.5 MHz, using 903 individual pointings with 15 minutes observations. The beam size at the location of SPT2349–56 is $24'' \times 13''$. We retrieved the ASKAP image surrounding SPT2349–56 using the cutout server. At the decl. of SPT2349–56 the achieved rms sensitivity is $189 \mu\text{Jy}$. The rms is similar in the ASKAP images around the other 22 lensed SPT-SMGs, although the actual sensitivity depends on proximity to other nearby bright radio sources (see Appendix C). The SPT2349–56 ATCA-detected source is not cataloged in the RACS, but we find a 4.6σ peak approximately $5''$ from the ATCA source (shown in Figure 1).

2.4. ALMA Observations

Extensive ALMA properties of SPT2349–56 sources B, C, and G have already been published (Miller et al. 2018; Hill et al. 2020; Rotermund et al. 2021). Here, we present several new ALMA observations (Table 2), supporting our measurements of line emission in the context of searching for AGNs.

ALMA Band 4 imaging (150 GHz) was obtained under three different programs in Cycles 3, 6, and 8, all targeting the brightest peak of the LABOCA source, and tuned to place CO(7–6) ($\nu_{\text{rest}} = 806.652 \text{ GHz}$) and [C I](2–1) ($\nu_{\text{rest}} = 809.34 \text{ GHz}$) in the upper sideband, and para-H₂O(2₁₁–2₀₂) ($\nu_{\text{rest}} = 752.033 \text{ GHz}$) in the lower sideband.

²⁴ <https://github.com/IanHeywood/oxkat>

²⁵ <https://github.com/ratt-ru/tricolor>

²⁶ The name means “shared skies and stars” in the local indigenous language, Wajarri Yamatji.

Table 3
Continuum and Line Properties of B, C, and G

ID	R.A., decl.	S_{147} (μJy)	S_{231} (μJy)	$F_{\text{CO}(16-15)}$ (Jy km s^{-1})	$F_{\text{CO}(11-10)}$ (Jy km s^{-1})	$F_{\text{CO}(7-6)}$ (Jy km s^{-1})	$F_{\text{H}_2\text{O}}$ (Jy km s^{-1})	F_{OH} (Jy km s^{-1})	$F_{[\text{C I}](2-1)}$ (Jy km s^{-1})
B	23:49:42.79, -56:38:24.0	589 ± 15	3322 ± 156	0.12 ± 0.05	0.23 ± 0.06	0.73 ± 0.05	0.22 ± 0.02	0.93 ± 0.11	0.46 ± 0.03
C	23:49:42.84, -56:38:25.1	336 ± 11	1810 ± 118	0.10 ± 0.06	0.26 ± 0.05	0.61 ± 0.03	0.15 ± 0.01	0.83 ± 0.08	0.35 ± 0.03
G	23:49:42.74, -56:38:25.1	181 ± 23	136 ± 9	0.10 ± 0.05	0.08 ± 0.05	0.18 ± 0.02	0.02 ± 0.01	0.22 ± 0.06	0.10 ± 0.02

Notes. S_{147} and S_{231} are the continuum flux densities at 147 and 231 GHz, respectively, while the other columns provide various line strengths (the line is indicated by the subscript). The OH doublet arises from blended hyperfine triplets centered at 1835 and 1838 GHz, and the H₂O line is the para-2₁₁-2₀₂ line.

The Cycle 3 program 2015.1.01543.T (PI: K. Lacaille) was observed on 2016 March 20. The array was in the C36-2/3 configuration with baselines ranging from 15 to 460 m, and provided a naturally weighted synthesized beam size of 0".88. Pallas and J2343–5626 were used to calibrate the amplitude and phase, respectively. The Cycle 6 program (2018.1.00058.S; PI: S. Chapman) observations were obtained on 2018 October 3 in the C43-6 array configuration with baseline lengths of 15–2500 m, giving a naturally weighted synthesized beam size of 0".28. J2056–4714 was used to calibrate the amplitude, while J2357–5311 was used to calibrate the phase. Lastly, the Cycle 8 program (2021.1.01313.S; PI: R. Canning) observations were obtained on 2022 July 27. These observations used the C-6 array configuration with baselines of 15–2500 m, giving a naturally weighted synthesized beam size of 0".27. J2357–5311 was used to calibrate the amplitude, while J2336–5236 was used to calibrate the phase.

The Cycle 8 program (2021.1.01313.S) also observed CO(11–10) ($\nu_{\text{rest}} = 1267.01$ GHz) and continuum at about 230 GHz in Band 6. These observations, carried out on 2022 September 1, used the C-4 array configuration with baselines of 15–784 m, giving a naturally weighted synthesized beam size of 0".47. J2357–5311 and J2258–2758 were used to calibrate the amplitude, while J2357–5311 and J2336–5236 were used to calibrate the phase.

We also make use of previously published Band 7 (345 GHz) ALMA Cycles 5 and 6 observations (Hill et al. 2020). The deep 0".5 resolution (i.e., synthesized beam) Cycle 5 data contain the CO(16–15) line ($\nu_{\text{rest}} = 1841.35$ GHz) and an OH doublet; each of the doublets is actually composed of a triplet whose frequencies are about 0.01 GHz separated, which is completely unresolved by our spectral resolution, so we consider the OH line to be a doublet. The mean frequencies of the doublet are $\nu_{\text{rest}} = 1837.80$ GHz and $\nu_{\text{rest}} = 1834.74$ GHz. These lines are present in the upper sideband, which was not previously analyzed or published. The high-resolution Cycle 6 data described by Hill et al. (2020) has a synthesized beam of about 0".2 and is here used to further analyze kinematics through a moment analysis of the [C II] line (Section 3.3).

All the data were calibrated using the standard observatory-supplied calibration script. Imaging was done using the CASA task `tclean`, using a Briggs' weighting with a robustness parameter of 0.5, and in all cases channel widths were averaged down to a common 15.625 MHz. The Cycles 6 and 8 observations covering the CO(7–6), [C I](2–1), and H₂O lines were combined in uv space and then imaged together, while the Cycle 3 observation was imaged separately. We chose this approach as the two data sets did not overlap entirely in frequency, which led to artefacts in the imaging step. The higher-resolution Cycles 6 and 8 data cubes were then convolved to match the resolution of the Cycle 3 data (about

0".88). The continuum was subtracted using the task `imcontsub` after flagging all channels expected to contain line emission based on previously detected [C II] lines given in Hill et al. (2020). At each spatial pixel, `imcontsub` extracts a one-dimensional spectrum and calculates the average over all channels not flagged by the user, then subtracts this average and returns a continuum-subtracted data cube.

The same apertures used by Hill et al. (2020) to extract [C II] line strengths and 350 GHz continuum flux densities were applied to sources B, C, and G in order to extract one-dimensional spectra for each line. The Cycle 3 and Cycles 6 and 8 CO(7–6), [C I](2–1), and H₂O spectra were averaged to produce a final spectrum. Details on line strengths and continuum flux densities (including our procedure for deblending lines) are given in Appendix B, and the spectra are shown in Figures 9–11 in Appendix B. All new continuum flux densities and line strengths are listed in Table 3, and the new continuum measurements are also shown in Figure 2.

3. Results

3.1. Identifying and Characterizing Radio Sources

We first searched for radio sources at the positions of known ALMA and optically identified members of the SPT2349–56 protocluster. There is one strong radio detection at 2.2 GHz ($S_{2.2} = 214 \mu\text{Jy}$) found near the SPT2349–56 core with ATCA (detected at 8σ), which corresponds to a (5σ) detection with ASKAP at 888 MHz and a strong detection with MeerKAT at 816 MHz (Figure 1 and Table 1). The ATCA source, with a smallest beam, encompasses the bright central ALMA sources, named B, C, and G based on their rank-ordered 850 μm flux densities Miller et al. (2018).²⁷ The MeerKAT and ASKAP sources are consistent with this position. It is unclear from positional uncertainty and beam sizes whether the emission comes from all three galaxies or just a single source. Irrespective of this, the strong radio emission would be in excess from that expected from the far-infrared (FIR)–radio correlation (Helou et al. 1985). We analyze these issues in detail in Section 3.2.

There are no other significant ($>3\sigma$) ATCA detections of any known protocluster members (Figure 1). The FIR–radio correlation for star-forming galaxies (Helou et al. 1985; Ivison et al. 2010) would imply $S_{2.2} \approx 12 \mu\text{Jy}$ for a $S_{850} = 5$ mJy source at $z = 4.3$. The 10 brightest SPT2349–56 SMGs (excluding B, C, and G) span 0.8–15 mJy, with an average of 4.7 mJy. Thus even the brightest SMGs would only be expected to be at the 1σ level in our ATCA map. A radio-

²⁷ These three sources are named C3, C6, and C13 in Hill et al. (2020) based on their rank-ordered [C II] line strength.

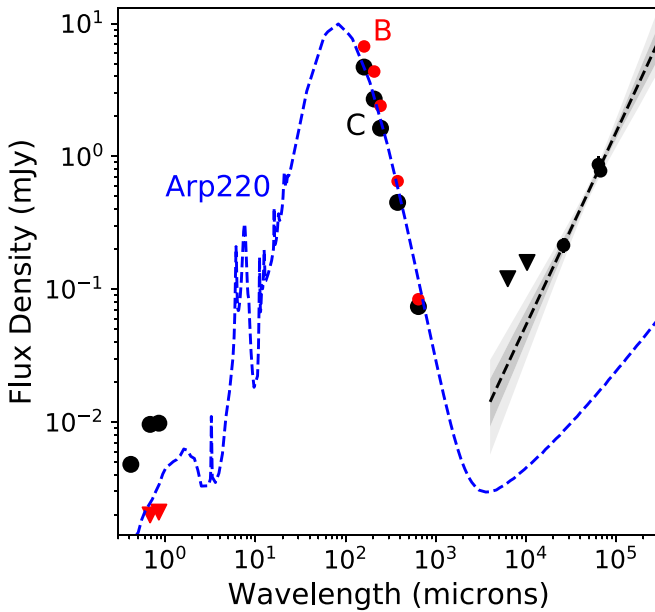


Figure 2. Spectral energy distribution showing the ATCA, ASKAP, and MeerKAT radio detections at rest wavelengths, where error bars are smaller than most symbols (the 5σ ASKAP radio detection is consistent with MeerKAT). Also shown are the ALMA flux densities of the brightest two of the central SMGs (B, red circles; C, black circles), along with rest-frame optical photometry of ALMA source C (as in Figure 1), which was modeled with a $3 \times 10^{11} M_{\odot}$ stellar mass fit (Rotermund et al. 2021). Source B is undetected at these wavelengths (red limits). The Arp220 SED (dashed blue line) is normalized to the submm photometry, revealing that the SPT2349 BCG galaxy complex has significant excess in radio above the far-infrared (FIR)–radio correlation for star-forming galaxies. The 5.5 and 9 GHz limits are shown at 3σ . The radio spectral index is constrained to $\alpha = -1.45 \pm 0.16$ (fitted line) by the MeerKAT and ASKAP detections, and consistent with the upper limits. The gray shadings show the 1 and 2σ uncertainties in the fit (Appendix C); an Arp220 $\alpha = -0.8$ spectral index is ruled out at the 5σ level by the 5.5 GHz nondetection.

stacking analysis on these remaining 10 brightest SMGs finds $(11.0 \pm 10.0) \mu\text{Jy}$, which is completely consistent with the average 2.2 GHz emission expected from the FIR–radio correlation, $\langle S_{2.2} \rangle = 12 \mu\text{Jy}$. Stacking on all 40 known cluster members yields $-5.0 \pm 5.8 \mu\text{Jy}$.

We then consider if there might be other radio sources in SPT2349–56 that could be cluster members. We searched for robustly detected radio sources in the surroundings of SPT2349–56 out to 1 Mpc in projection ($140''$ in radius) from the core, roughly the region studied with ALMA by Hill et al. (2020). We find one ATCA source above 5σ , ID2 (see Figure 1) in Table 1. ID2 is identified to a bright star, and is also detected by ASKAP and MeerKAT. A third source, ID3 (Figure 1), is only detected by MeerKAT. It has a clear optical and submm counterpart and a spectroscopic redshift of 0.66 from ^{12}CO lines in the ALMA data.

We thus focus on the properties of the central ID1 radio source, starting with the positional uncertainty, $\Delta\alpha$. From Condon (1997), we can derive the synthesized beam positional uncertainty for the ATCA, ASKAP, and MeerKAT detections, assuming that the beam is a single two-dimensional Gaussian with an rms “width” $\sigma = \text{FWHM}/2.354$ in each coordinate. In the limit where centroiding uncertainty dominates over systematic astrometry errors and for uncorrelated Gaussian noise, we have $\Delta\alpha = 0.6 (S/N)^{-1} \text{FWHM}$. For the ATCA, MeerKAT, and ASKAP sources in SPT2349–56, we have confirmed that the source size and PA is indistinguishable from other brighter, unresolved sources in the field, in agreement

with the synthesized beam. We conclude that the SPT2349–56 radio source ID1 is unresolved with our current data.

For the ATCA source (ID1) detected at $S/N = 8$ and a beam size of $4'' \times 8''$ (PA = 27 deg east of north), the positional uncertainty is therefore $0.''3 \times 0.''6$. For the ASKAP source detected with a S/N of 4.6 and a beam size of $24'' \times 13''$ (PA = 89 deg east of north) the positional uncertainty is therefore $3.''0 \times 1.''7$. For the MeerKAT source detected with a S/N of 64 and a circular beam size of $11''$ the positional uncertainty is therefore only $0.''1$ and, as with the ATCA source, lies between ALMA sources B and C, leaving the precise association ambiguous. However, there is a $5.''1$ roughly northern offset between the ATCA and ASKAP sources, which is consistent at the joint 2σ level. Comparison of our wider-field ATCA map and the ASKAP RACS map reveals that the majority of the sources show good astrometric alignment, but we also identify a few other ATCA sources with ASKAP counterparts with several arcsecond offsets (see Appendix A). In two cases there is a robust association of the ATCA position to other cataloged objects (from the Two Micron All Sky Survey), suggesting the offset to the ASKAP position is likely due to measurement error. For ID1, the more robust ATCA and MeerKAT positions and association to the B, C, and G galaxies in SPT2349–56 is the most likely interpretation, with the ASKAP source being assumed to be entirely related to the ATCA and MeerKAT sources for the purposes of deriving a radio spectral index.

3.2. Physical Interpretation of ID1

We first constrain the radio spectral index to estimate and compare luminosities between sources. The radio source ID1 has a steep spectrum with an index of $\alpha = -1.45 \pm 0.16$, constrained by the MeerKAT 816 MHz, ASKAP 888 MHz detection, and the ATCA nondetections at 5 and 9 GHz. The uncertainty can be estimated by propagation of errors on the two frequencies (first combining ASKAP and MeerKAT in quadrature) as follows:

$$\Delta\alpha = \frac{\sqrt{\text{SNR}_{2.2}^{-2} + \text{SNR}_{852}^{-2}}}{\ln(2.2/0.85)}. \quad (1)$$

However, we adopt here a Markov Chain Monte Carlo (MCMC) method (described in Appendix C) to assess the uncertainty for any number of spectral measurements, and show this distribution in Figure 2. The spectrum is too steep to be consistent with synchrotron radiation due to shock acceleration of cosmic-ray electrons from supernovae (i.e., star formation), where Thomson et al. (2014) recently constrained $\alpha = -0.79 \pm 0.06$ specifically for high- z SMGs. The steep SPT2349–56 spectrum seems to demand an AGN interpretation.

The radio luminosity can then be assessed by assuming it is associated with one of the central SPT2349–56 galaxies at $z = 4.3$. With a specific luminosity of $L_{2.2} = (4.4 \pm 0.3) \times 10^{25} \text{ W Hz}^{-1}$, it is far larger than expected from star formation through the FIR–radio correlation. For reference, the FIR–radio correlation for star-forming galaxies (Ivison et al. 2010) would imply $L_{2.2} = 2.4 \times 10^{24} \text{ W Hz}^{-1}$ for a similar $S_{850} = 5 \text{ mJy}$ source at $z = 4.3$. Adopting the measured spectral index above, the radio excess increases to over a factor 100 at a rest frame of 1.4 GHz, with $L_{1.4, \text{rest}} = (2.2 \pm 0.2) \times 10^{26} \text{ W Hz}^{-1}$. This

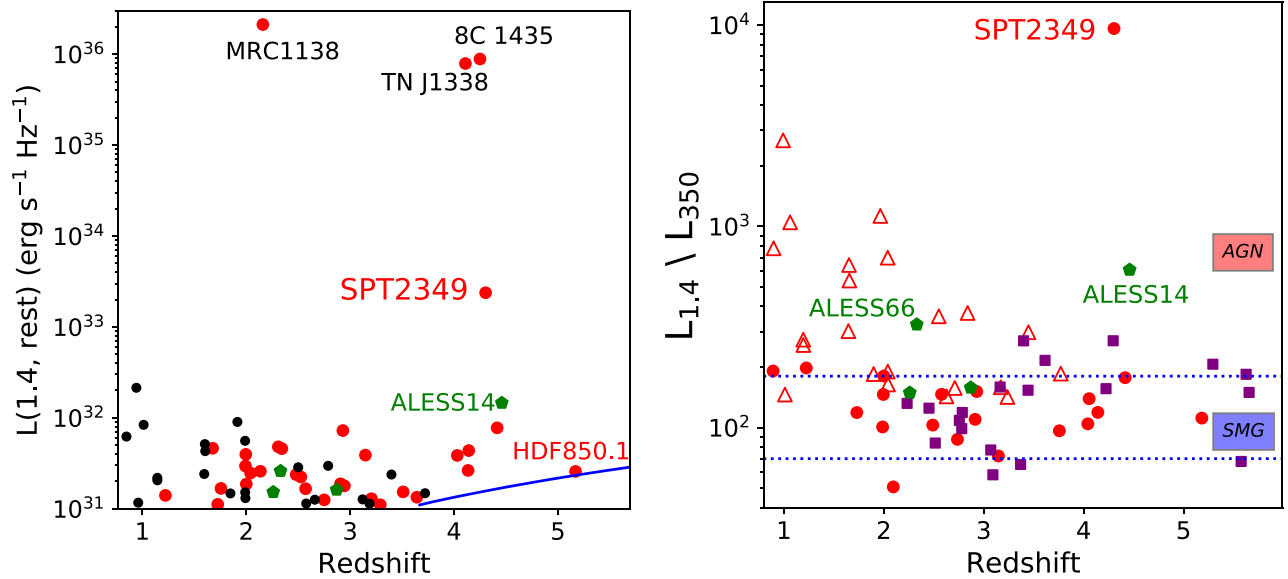


Figure 3. Left: redshift vs. 1.4 GHz radio power using the GOODS-N sample (Barger et al. 2017) and radio-excess candidates from the ALESS sample (Thomson et al. 2014, green circles). Symbols are as follows: red circles show sources detected above the 3σ level at $850 \mu\text{m}$, while black circles show sources not detected at this level. SPT2349–56 has about 10 times more radio power than any radio source found in GOODS-N, although it has more than 500 times lower radio power than other well-studied radio-loud galaxies (labeled) that were used to identify high-redshift protoclusters. Right: rest-frame 1.4 GHz luminosity over 350 GHz luminosity vs. redshift for the submm sources with spectroscopic redshifts in GOODS-N (red circles), and lower limits on radio sources undetected in the submm (red triangles). Also shown is the ATCA survey of lensed SPT-SMGs described in Appendix C (purple squares). The blue dashed line region shows where the submillimeter luminosities and radio luminosities produce consistent estimates of SFRs. None of the GOODS-N SMGs show any excess radio emission over the FIR–radio relation, while two of the ALESS sources do have a clear excess. Some of the higher-redshift SPT-SMGs show a marginal radio excess, discussed in Appendix C. SPT2349–56 is about 100 times higher than the median relation at rest 1.4 GHz. The HzRGs lie about 500 times higher with their measured $S_{850} = 6\text{--}12$ mJy.

strong radio excess suggests the presence of an AGN (e.g., Guidetti et al. 2017); however, the radio emission is still distinctly less luminous than powerful radio galaxies, like those residing in other structures studied at these redshifts, by a few orders of magnitude (Figure 3). MRC 1138, for instance, is almost 1000 times more powerful in radio, and it is also hosted by the obvious BCG of the protocluster (e.g., Hatch et al. 2009).

We then compare SPT2349–56 to radio sources from the literature. In Figure 3, the redshift versus radio power is shown using the 0.3 deg^2 GOODS-N Very Large Array sample (Barger et al. 2017), which is highly complete in spectroscopic redshift. We compute the rest-frame radio luminosity using the equation

$$L_{1.4} = (4\pi d_L^2 S_{1.4}/10^{29})(1+z)^{-(\alpha+1)} \text{ erg s}^{-1} \text{ Hz}^{-1}, \quad (2)$$

where d_L is the luminosity distance (in centimeters) and $S_{1.4}$ is the flux density in units of microjanskys observed at 1.4 GHz. This equation assumes $S_\nu \propto \nu^\alpha$, and we adopt a radio spectral index of $\alpha = -0.8$ (Ibar et al. 2010) for the GOODS-N sources and the measured α for SPT2349–56 and the literature HzRG sources (in fact all very close to -1.6). Shown for comparison are several well-studied HzRGs that were used as beacons to uncover massive galaxy overdensities: MRC 1138 (Large et al. 1981; Seymour et al. 2012), TN J1338 (De Breuck et al. 1999), and 8C 1435 (Lacy et al. 1994). SPT2349–56 has around 10 times more radio power than any radio source found in GOODS-N, but it has less than 500 times the radio power of these HzRGs.

Figure 3 also directly assesses the departure of SPT2349–56 from the radio–FIR correlation by plotting the luminosity ratio of 1.4–350 GHz versus redshift for all GOODS-N submm

sources with spectroscopic redshifts (Barger et al. 2014; A. Huber 2023, in preparation). All of the submm sources in GOODS-N are radio detected, even at $z = 5.2$, and the submm luminosity and radio luminosity produce consistent estimates of the SFRs for all sources—there is no sign of AGNs from their radio emission. A similar analysis of the subset of gravitationally lensed SPT-SMGs also observed from ATCA in this program (Appendix C) suggests the majority (87%) also follow this relation; however, there are three very significant outliers in this sample, which is most likely attributed to an AGN contribution from the foreground lensing galaxy (discussed further in Appendix C). SPT2349–56 is an outlier by a factor of about 100 from this envelope (assuming the radio emission is coming exclusively from ALMA source C). The HzRGs shown in the left panel of Figure 3 have comparable $S_{850} = 6\text{--}12$ mJy to other SMGs shown (e.g., De Breuck et al. 1999; Dannerbauer et al. 2014), and would remain about 500 times above SPT2349–56 in the radio/submm ratio plot in the right panel. By contrast, the GOODS-N radio sources without submm detection rise significantly above this envelope, into the AGN regime.

Thomson et al. (2014) have used the deep Jansky Very Large Array (1.4 GHz) and the Giant Metrewave Radio Telescope (610 MHz) to study the 76 ALMA-identified SMGs in the CDFS field (the ALESS survey; e.g., Simpson et al. 2014). They find four SMGs whose radio-FIR values are $>2\sigma$ above the sample median, which they classify as potential AGNs. The most robust of these (ALESS 066.1) is a strong X-ray source with an inverted radio spectrum ($\alpha > 0.51$). Of the remaining three, one (ALESS 014.1) has a flat radio spectrum ($\alpha > -0.1$) and an obviously high radio luminosity, while the other two (ALESS 094.1 and ALESS 118.1) have spectral index limits consistent with star formation ($\alpha \sim -0.8$). We show these four SMGs in Figure 3, where it is clear that none are comparable to

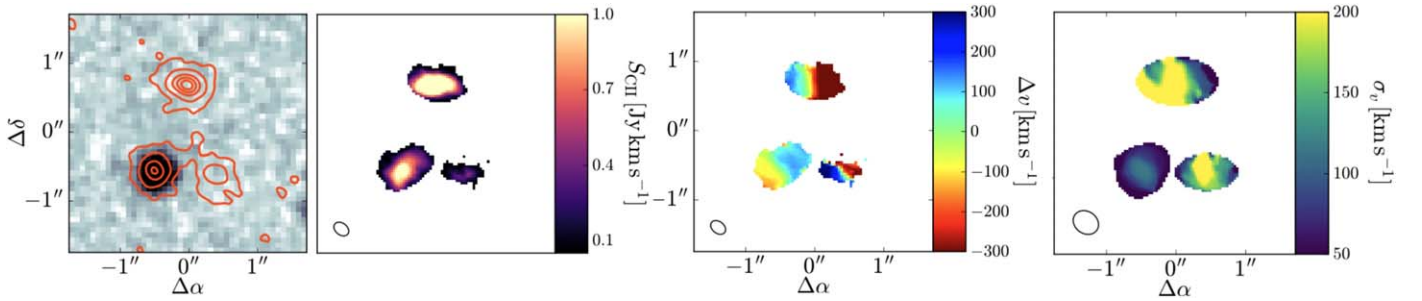


Figure 4. Moment maps of B, C, and G. Left: 850 μm continuum (red contours) from high-resolution ($0''.3$) combined Cycle 5 and Cycle 6 ALMA data (Hill et al. 2020), shown overlaid three-orbit HST F160W imaging (Hill et al. 2022). Mid-left: [C II] moment 0 maps from Cycle 6 high-resolution ALMA data. Mid-right: [C II] moment 1 maps (in velocity units) from Cycle 6 ALMA data, with the zero velocity centered at the peak of each galaxy’s [C II] emission. All three sources show a clear velocity gradient (listed in Table 4, along with dynamical mass comparisons). Right: [C II] moment 2 maps (in velocity units) are shown from lower-resolution data to increase the S/N, revealing centrally concentrated dispersions. In all panels, the synthesized beam FWHM is shown in the bottom-left corner.

SPT2349–56 in radio luminosity or departure from the FIR–radio relation. In fact, two of the four are not at all unusual in their properties relative to the other samples.

Radio emission provides an extinction-free probe of AGNs (which even X-ray cannot claim, since practical sensitivity limits preclude the detection of the most obscured, Compton-thick AGNs with $N_{\text{H}} > 10^{24} \text{ cm}^{-2}$). Traditionally, radio AGNs are divided into two subsets (Padovani 2017): (i) radio-loud AGNs $L_{1.4} > 10^{24} \text{ W Hz}^{-1}$, which exhibit steep spectrum radio jets and lobes on kiloparsec scales (Yun et al. 1999); and (ii) radio-quiet AGNs, with flat-spectrum, lower-luminosity radio emission, typically contained within a compact, several parsec, core (Blundell & Kuncic 2007). SPT2349–56 is solidly a radio-loud AGN, whereas most of the other candidate AGNs found in the surveys described above (GOODS-N and ALESS) cannot clearly be defined as such.

3.3. Resolved Properties of the “BCG” Sources

Given the radio detection in SPT2349–56, it is of interest to assess the properties of the B, C, and G ALMA sources, and to compare them to other protocluster members. As noted, these are three very submm-luminous sources in the core region ($S_{850} = 6.7 \text{ mJy}$ for B, 4.7 mJy for C, and 1.3 mJy for G), with only source A being brighter, although two even more luminous sources are present in the northern extension (sources N1 and N2; Hill et al. 2020).

The most distinguishing features of this trio (beyond their flux-ordered source names serendipitously spelling out “BCG”) are their locations near the center-of-mass of the cluster core, and their immediate environment. They are very close neighbors (they lie within an arcsecond of each other), and are likely to be interacting. Further, there is a notable arc seen in [C II] surrounding the three galaxies (Hill et al. 2020; N. Sulzhanauer 2023, in preparation). Source C does distinguish itself with an anomalously narrow [C II] and CO(4–3) line width for its luminosity (Hill et al. 2020). Rotermund et al. (2021) performed a mass budget analysis of SPT2349–56 galaxies and identified C as a significant outlier from the sample in its $M_{\text{dyn}}/M_{\text{gas}}$ ratio inferred from the narrow CO(4–3) line width and large luminosity. This is similar to many high- z QSOs (e.g., Narayanan et al. 2008; Walter et al. 2009; Hill et al. 2019) where selection effects favoring face-on orientation offer viable explanations. It is also noteworthy that source C has by far the largest stellar mass of any cluster member ($>10^{11} M_{\odot}$; Rotermund et al. 2021; Hill et al. 2022). It is associated with a bright and very compact Hubble Space

Telescope (HST) F160W source (Hill et al. 2022), as shown in Figures 1 and 4, and has been suggested to be the seed of a growing BCG galaxy in this ongoing mega-merger (Rennehan et al. 2020).

3.3.1. [C II] Kinematics

We consider here a more detailed analysis of the kinematic properties of the B, C, and G galaxies. Using high-resolution Cycle 6 [C II] data (Hill et al. 2020), which has a synthesized beam of about $0''.2$, we construct moment 0, 1, and 2 maps of the B, C, and G sources and analyze the resolved velocity and dispersion fields. We use the CASA task `immoments`, focusing on channels between $\pm 3\sigma$ of the best-fit [C II] line, and masking pixels < 4 times the rms per channel. Since second moments are particularly sensitive to noise (being a squared term), we use uv -combined Cycles 5 and 6 data cubes (described in Hill et al. 2020) to calculate the moment 2 maps; for reference, the resolution of the combined data is about $0''.3$. The results (moments 0, 1, and 2) are shown in Figure 4.

All three sources show a clear velocity gradient and resolved, centrally concentrated dispersion, characteristic of rotationally supported disks. From these velocity gradients and velocity dispersion maps we extract peak-to-peak velocities, $V_{\text{p-p}}$, and central velocity dispersions, FWHM_{cen} . We draw a line along the semimajor axis of each galaxy, then from the moment 1 map calculate the velocity difference between the two ends, and from the moment 2 map extract the velocity dispersion at the midpoint of the line. We find that moving the PA of the line by ± 10 deg and moving the midpoint of the line by 5 pixels results in a peak-to-peak velocity change of $\pm 50 \text{ km s}^{-1}$ and a central velocity dispersion change of $\pm 10 \text{ km s}^{-1}$ ($\pm 20 \text{ km s}^{-1}$ in FWHM), so we quote these as our uncertainties. The results are given in Table 4, multiplied by a factor of $2\sqrt{2 \ln 2}$ to estimate a FWHM.

We use these peak-to-peak velocities and central dispersions to estimate masses assuming a disk model, with the enclosed dynamical mass given by

$$M_{\text{dyn,disk}} [M_{\odot}] = 2.35 \times 10^5 [V_{\text{p-p}} / \langle \sin(i) \rangle]^2 R, \quad (3)$$

where $V_{\text{p-p}}$ is the peak-to-peak velocity in kilometers per second, R is the radius in kiloparsecs, and i is the inclination angle of the galaxy. We adopt a mean inclination suitable for a collection of randomly oriented disks of $\langle \sin(i) \rangle = \pi/4 \simeq 0.79$ (see Law et al. 2009), and we use the half-light radii from Hill et al. (2022), estimated by fitting Sérsic

Table 4
Physical Properties of B, C, and G

ID	SFR _{H₂O} ($M_{\odot} \text{ yr}^{-1}$)	$S_{850}/F_{\text{H}_2\text{O}}$ ($10^{-3} \text{ km}^{-1} \text{ s}$)	SFR _{LIR} /SFR _{H₂O}	$V_{\text{p-p}}$ (km s^{-1})	$M_{\text{dyn,disk}}$ ($10^{10} M_{\odot}$)	FWHM _{cen} (km s^{-1})	$M_{\text{dyn,cen}}$ ($10^{10} M_{\odot}$)	FWHM _{int} (km s^{-1})	$M_{\text{dyn,int}}$ ($10^{10} M_{\odot}$)
B	1100 ± 410	31 ± 3	0.8 ^{+0.5} _{-0.4}	600 ± 50	18.2 ± 2.2	540 ± 20	11.0 ± 0.8	612 ± 10	14.0 ± 0.5
C	750 ± 280	31 ± 2	0.8 ^{+0.5} _{-0.4}	240 ± 50	2.9 ± 0.8	280 ± 20	2.9 ± 0.4	358 ± 5	4.7 ± 0.2
G	80 ± 60	65 ± 23	2.3 ^{+2.0} _{-1.8}	690 ± 50	18.1 ± 2.5	520 ± 20	7.6 ± 0.8	901 ± 54	22.8 ± 2.8

Notes. SFR_{H₂O} is the SFR estimated using Equation (5), $S_{850}/F_{\text{H}_2\text{O}}$ is the ratio of 850 μm continuum flux density (from Hill et al. 2020) to H₂O line strength, and SFR_{LIR}/SFR_{H₂O} is the ratio of the FIR-derived SFR (from Hill et al. 2020) to the H₂O-derived SFR. $V_{\text{p-p}}$ is the peak-to-peak velocity from moment 1 maps, while FWHM_{cen} is the central velocity dispersion (multiplied by $2\sqrt{2\ln 2}$) from moment 2 maps (see Figure 4), and FWHM_{int} is the width of the [C II] line after fitting a single Gaussian to the lines shown in Figures 9–11. $M_{\text{dyn,disk}}$ is the dynamical mass derived using $V_{\text{p-p}}$ and a disk model (Equation (3)), while $M_{\text{dyn,cen}}$ and $M_{\text{dyn,int}}$ are dynamical masses derived using the velocity dispersion measurements and Equation (4).

profiles to the high-resolution ALMA [C II] moment 0 images. The results are given in Table 4.

The dynamical masses were derived previously (Rotermund et al. 2021) from the unresolved velocity dispersions, using the width of the integrated [C II] lines shown in Figures 9–10, with an assumption about the structure of the source based on the virial theorem, using the relation

$$M_{\text{dyn}}[M_{\odot}] = 2.81 \times 10^5 \text{FWHM}^2 R, \quad (4)$$

where FWHM is a one-dimensional velocity dispersion (multiplied by a factor of $2\sqrt{2\ln 2}$) in kilometers per second, and R is the radius of the virialized structure. First, we use the resolved central velocity dispersion, FWHM_{cen}, adopting the [C II] size measurements from Hill et al. (2022) and the central resolved velocity dispersions from the moment 2 maps (Table 4). Next, we use the width of the integrated [C II] line, FWHM_{int}, obtained by fitting a single Gaussian model to the [C II] spectra shown in Figures 9–11 and given in Table 4, again using Equation (4) and the same [C II] size measurements. The resulting dynamical masses are provided in Table 4.

Considered in the context of a disk model, source C does show a similar dynamical mass comparing both its central and integrated velocity dispersion (Table 4, and Rotermund et al. 2021); however, it still appears to have substantially lower mass (6 times lower) than B from any kinematics analysis. Inclination is reasonably constrained, since the aspect ratio of these galaxies is resolved by ALMA. While it remains an uncertainty in any mass modeling, the aspect ratios of B and C are similar at ~ 1.8 (major to minor axis).

Sources B and G have similarly large inferred disk masses ($18 \times 10^{11} M_{\odot}$). However, the distinct double-horned profile of source G (Appendix B) is direct evidence for a rotating disk or bar-like structure at high inclination (explaining the broad velocity profile), while the profile for B is possibly due to a tidal torque in response to the interaction with C. Source G also has a higher aspect ratio (2.3, major/minor axes) in moment 1 than B and C, suggesting the disk is seen closer to edge-on. Explicitly using this higher implied inclination in Equation (3) brings down the disk mass estimate by 25%, more consistent with the much lower gas mass of G compared with B and C.

It is noteworthy that, in projection at least, B is counter-rotating relative to C. Several studies have predicted that mergers configured with counterrotating gas disks should lead to the most intense starbursts, and conditions for fueling the SMBHs (e.g., Mihos & Hernquist 1994, 1996; Di Matteo et al. 2007; Salomé et al. 2012).

3.3.2. Submillimeter Line Properties

We then consider line diagnostics to elucidate which of the three might be most likely to host the radio AGN. We first assess the [C II]/FIR ratio, which has been shown to highlight AGNs with a deficit compared with star-forming galaxies (e.g., Stacey et al. 2010). However, at high luminosities, both AGNs and SMGs (without obvious AGNs) exhibit similar deficits in the ratio. Hill et al. (2020) have shown that all three of B, C, and G are “deficit sources” in [C II]/FIR, inhabiting similar regions in the [C II]/FIR-to-FIR plot as many luminous AGNs. However, this work also showed that all 12 of the most luminous SMGs in SPT2349–56 have comparable [C II]/FIR ratios, and none of these are obviously AGNs from any available diagnostics.

One possibility to consider is that the FIR estimates are being affected by an AGN in one of B, C, or G. Since the shortest wavelength measured by ALMA is 160 μm in the rest frame, the peak of the spectral energy distribution (SED) is not sampled, and there is little constraint on whether the dust might be substantially hotter than the $T_{\text{d}} \approx 40$ K estimated in Hill et al. (2020). To test this, we make use of the para-H₂O(2₁₁–2₀₂) lines observed in the ALMA Band 4 data set (Table 3 and Figures 9–11). H₂O is strongly coupled to the FIR radiation field whether it is being produced by star formation or AGNs (Omont et al. 2013). Jarugula et al. (2021) compiled a sample of low- and high- z SMGs with para-H₂O(2₁₁–2₀₂) measurements (including two sources, SPT0346–52 and SPT0311–58, from the same parent sample as SPT2349–56), and found that a simple single-parameter scaling relation described the correlation between $L_{\text{H}_2\text{O}}$ and SFR (derived from FIR) of the form

$$\text{SFR} [M_{\odot} \text{ yr}^{-1}] = (2.07 \pm 0.75) \times 10^{-5} L_{\text{H}_2\text{O}} [L_{\odot}]. \quad (5)$$

A simple test is to first take the ratio of 850 μm continuum flux density to H₂O line strength, where measurement errors are mostly small. These values are given in Table 4, where we have used S_{850} values from Hill et al. (2020). Using the same modified blackbody SED as in Hill et al. (2020) to model the continuum flux density emission, a dust temperature of 40 K at a redshift of 4.3 means that $S_{850} = 1$ mJy corresponds to $115 M_{\odot} \text{ yr}^{-1}$, and so Equation (5) implies $S_{850}/F_{\text{H}_2\text{O}} = (42 \times 10^{-3}) \text{ km}^{-1} \text{ s}$; B and C sit significantly below this value, implying they might have higher FIR than currently estimated. In contrast, G is significantly above the relation, which could imply cooler dust and lower FIR than previously estimated. This would make G less of a deficit source in [C II]/FIR, and less likely to be considered an AGN by this criterion.

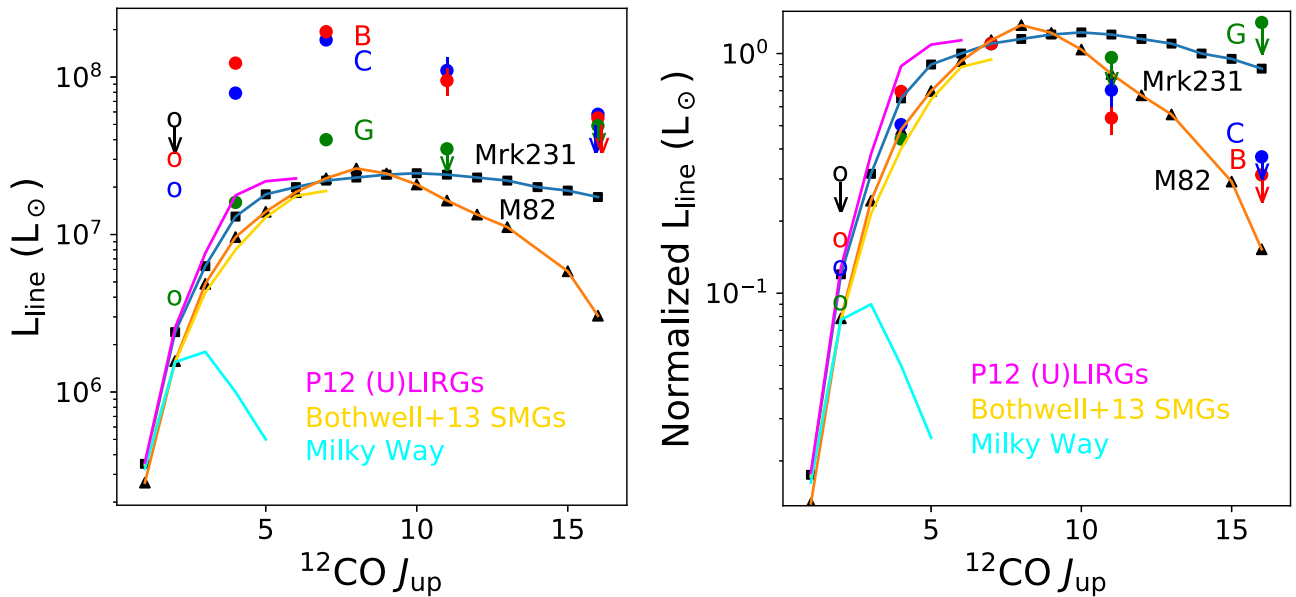


Figure 5. SLEDs for sources B, C, and G in the CO $J_{\text{upper}} = 2, 4, 7, 11,$ and 16 transitions (new data for the $J_{\text{upper}} = 7, 11, 16$ lines are shown in Appendix B). The ATCA detection of CO(2–1) (Miller et al. 2018) is shown as an upper limit as it is an unresolved measurement over the core region including at least B, C, and G. Open circles illustrate the $J = 2$ division if the luminosities scale from $J = 4$. We compare to the $L_{\text{FIR}} = 3 \times 10^{10} L_{\odot}$ AGN-dominated galaxy Mrk 231 (van der Werf et al. 2010), and the $L_{\text{FIR}} = 3 \times 10^{10} L_{\odot}$ starburst M82 (Kamenetzky et al. 2012), here normalized to Mrk 231 at CO(7–6). We also overlay the average (U) LIRG SLED from Papadopoulos et al. (2012, comparable to Mrk 231), the average $z \sim 2.5$ SMG from Bothwell et al. (2013, comparable to M82), and the Milky Way (Lagos et al. 2012). In the right panel the SPT2349–56 galaxies are also normalized to the CO(7–6) luminosity of Mrk 231 for comparison of the excitation curves. Source G is undetected in the $J_{\text{upper}} = 11$ and 16 lines, while B and C (shown as 2σ upper limits) are marginally detected in CO(16–15).

Using Equation (5), we can also estimate SFRs directly for B, C, and G using our measured para- $\text{H}_2\text{O}(2_{11}-2_{02})$ line strengths (Table 4), and compare these with the SFRs from the FIR (taken from Hill et al. 2020). These relations show the same behavior as our ratio of measurements above, that B and C both may have higher FIR (from hotter dust) than estimated from our current ALMA data. We note that systematic errors in converting to these physical quantities are large (as listed in Table 4).

We next consider the CO spectral line energy distribution (SLED), which can distinguish AGNs with high-excitation lines driven by X-ray-dominated regions (XDRs; e.g., van der Werf et al. 2010). Here, we present higher- J CO transitions (Section 2) than have previously been published in Miller et al. (2018). All of B, C, and G are well detected in CO(7–6) observations, while B and C are detected in CO(11–10). Remarkably, B and C may be marginally detected in CO(16–15) due to the sensitivity of the deep Band 7 ALMA data presented in Hill et al. (2020), although strictly they are upper limits. All the new line channel maps and one-dimensional spectra are shown in Appendix B. SLEDs are shown in Figure 5 from the available $J = 2, 4, 7, 11,$ and 16 transitions, and compared to AGN and starburst templates. The ATCA detection of CO(2–1) (Miller et al. 2018) is shown as an upper limit as it is an unresolved measurement over the core region including at least B, C, and G. However, for illustration we show the division into B, C, and G of the integrated $J = 2$ luminosity assuming they scale with the $J = 4$ fluxes. None of B, C, or G appear to have high-excitation SLEDs similar to AGNs like Mrk 231 (e.g., van der Werf et al. 2010), and are all similar to or less excited than M82 at high J (Kamenetzky et al. 2012), with the caveat that G has only upper limits beyond $J = 7$.

Source B has the highest-excitation SLED confirmed of the three, lying near the M82 SLED. Source B also has a stronger

cool/warm gas component similar to Mrk 231. However, all three are reasonably characterized with a combination of cool and warm star-forming photodissociation region components, and without significant XDR contributions. Detailed SLED modeling of SPT2349–56 sources will appear in a future contribution.

Finally, the $163 \mu\text{m}$ OH doublet in B, C, and G can be compared to Runco et al. (2020), who studied 178 local galaxies in six of the 14 OH transitions in the FIR range. They found the highest-frequency $\text{OH}_{163\mu\text{m}}$ (detected in 25 galaxies) is the only OH doublet that is always in emission, with most transitions often appearing in absorption. Runco et al. (2020) presented the correlations of the equivalent width, $\text{EW}(\text{OH})$, with various galaxy properties and line ratios, finding $\text{EW}(163 \mu\text{m})$ is not well established as a direct AGN indicator. For example, while galaxies with lower X-ray luminosities exclusively have low $\text{EW}(\text{OH})$, the full range of EW is seen for the highest X-ray luminosities (Runco et al. 2020). However, a strong correlation is found for $\text{EW}(\text{OH})$ with the ratio of AGN activity to SFR, suggesting this is a better predictor of $\text{EW}(\text{OH})$ than the total AGN power. In Figure 6, we compare the equivalent width, $\text{EW}(163 \mu\text{m})$, to local starbursts, LINERs, and Seyfert galaxies from Runco et al. (2020). The $\text{EW}(163 \mu\text{m}) = 0.076 \mu\text{m}$ and $0.095 \mu\text{m}$ measured for B and C, respectively, are among the highest found locally. (G is similarly high, but is only marginally detected in OH). Their $\text{EW}(163 \mu\text{m})$ are more similar to values in local Seyfert galaxies than starburst galaxies, the latter having $\text{EW}(163 \mu\text{m}) \sim 0.02\text{--}0.05 \mu\text{m}$. It is not yet clear at $z > 4$ what is “normal” for $\text{EW}(163 \mu\text{m})$, since the line has only before been detected locally. Indeed, the ICM conditions in $z > 4$ massive galaxies at these higher IR luminosities may lead to a higher $\text{EW}(163 \mu\text{m})$ even without AGNs. However, these results may provide initial evidence that B or C may in fact present as AGNs through some submm-wave diagnostics.

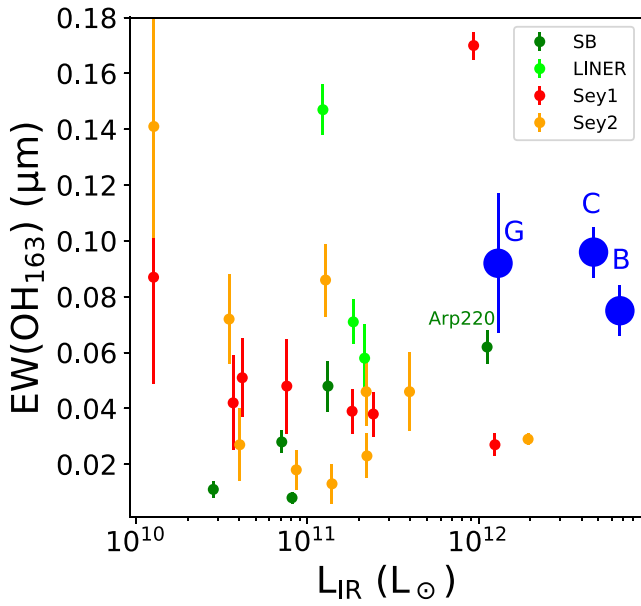


Figure 6. The equivalent width of the $\text{OH}_{163\mu\text{m}}$ doublet vs. IR luminosity. B, C, and G (blue circles) have similar values, although the error in G is large. We compare to all local galaxies detected in $\text{OH}_{163\mu\text{m}}$ from the compilation in Runco et al. (2020). Galaxies are color-coded by their classification as starbursts (SB, lime), LINERs (green), Seyfert-1 (red), and Seyfert-2 and intermediate types (orange), and Arp220 is singled out within the SB category. B, C, and G all appear above local starbursts, although all three local AGN types have a few examples this high.

3.3.3. Optical and Near-infrared Properties

Finally, we summarize optical and near-infrared (NIR) spectra taken with the Gemini and VLT observatories. A VLT XSHOOTER spectrum ($\lambda_{\text{obs}} = 0.35\text{--}2.4\ \mu\text{m}$) was obtained which targeted B and C (Rotermund et al. 2021), covering redshifted $\text{Ly}\alpha$ through $[\text{O II}]_{3727}$. No lines were detected. A VLT/MUSE spectral cube was used to extract one-dimensional spectra at the locations of each of B, C, and G (Apostolovski et al. 2023), but no lines are detected in any of these galaxies (nor any of the SPT2349–56 SMGs).

Nondetections are not particularly surprising given the faintness of the galaxies at $6450\ \text{\AA}$, the wavelength of redshifted $\text{Ly}\alpha$, where C has $S_{0.63\mu\text{m}} = 0.061\ \mu\text{Jy}$, while B and G are undetected to $S_{0.63\mu\text{m}} < 0.01\ \mu\text{Jy}$ (Rotermund et al. 2021; Hill et al. 2022). The difficulty of spectroscopy in the NIR at $19768\ \text{\AA}$ in the vicinity of the redshifted $[\text{O II}]_{3727}$ means these limits on line equivalent widths are also not particularly constraining. Nonetheless, strong AGNs often exhibit detectable high-excitation lines in optically faint, obscured SMG hosts (Chapman et al. 2003, 2004, 2005; Danielson et al. 2017), and it is surprising that this AGN in SPT2349–56 eludes all optical and NIR spectral detection.

3.3.4. Concluding Remarks

Thus while the radio observations do not have sufficient spatial resolution to uniquely identify one of the three galaxies as the AGN, the source properties themselves suggest source C could be a likely host, considering mainly its large stellar mass, along with narrow emission lines and high $\text{EW}(\text{OH})$. Sources with similar radio luminosities in the local Universe are typically found in massive hosts. However, the more FIR-luminous and much more dust-obscured source B might also be

a possible host for the AGN, given the large dynamical mass from kinematic modeling and the higher-excitation SLED. Of course, all three SMGs could have AGN components at the same time. The fact that they are likely strongly interacting dispels the typical duty-cycle arguments that would disfavor this scenario. To make progress, we will need deeper radio data with better resolution, and sensitive infrared (IR) spectroscopic observations now possible with the JWST.

4. Discussion

4.1. Inferring AGN Properties from Radio Power

4.1.1. Jet Power and Energy Input to the ICM

Radio jets are thought to provide an important feedback mode in galaxy clusters by preventing the cooling of hot (X-ray) gas surrounding central galaxies (e.g., McNamara & Nulsen 2012). This is referred to as “jet-mode” feedback and is associated with radio sources characterized by radiatively inefficient accretion. However, radio jets can also drive massive gas outflows on galactic scales, another signature of AGN feedback.

A theoretical relation between radio luminosity and radio jet power was determined by Willott et al. (1999), and can be used to estimate the kinetic energy output of AGNs (e.g., Hardcastle et al. 2007). The jet power can be estimated by assuming that the mechanical power of the jet can be approximated as the energy of the detected radio cavity averaged over some timescale (e.g., Birzan et al. 2004). The X-ray-detectable “cavities” that result from AGN jet activity (O’Sullivan et al. 2011) allow us to quantify the heating experienced by the ICM. The energy contained in these cavities comes from the product of the pressure and volume (pV) over the cavity. This is the work done by the jet to create the cavity, and the internal energy of the radio lobes. Under the assumption that the cavity is dominated by relativistic plasma, this becomes $4pV$. Dividing the energy of the cavity by the cavity age gives the power, P_{cav} .

Thus the most direct inference we can make from the radio properties of SPT2349–56 adopts a relatively tight correlation observed between radio power and cavity power (Cavagnolo et al. 2010; O’Sullivan et al. 2011; Panessa et al. 2015), where a fitted relation follows

$$\log P_{\text{cav}} = (0.35 \pm 0.07) \log L_{1.4} + (1.85 \pm 0.10), \quad (6)$$

yielding $P_{\text{cav}} = (3.3 \pm 0.7) \times 10^{38}\ \text{W}$. This is strictly a lower limit to the jet power, and therefore energy injection into the ICM. The true jet power depends on how the radio cavity is inflated (as described in Nusser et al. 2006), with some energy from the jet being carried away by shocks. The relation of $L_{1.4}$ to P_{cav} is still affected by uncertainties due to the assumption that the cavity is dominated by relativistic plasma and the detectability of cavities within the sample used in O’Sullivan et al. (2011), as discussed in their work.

This jet power is a sizable amount of energy, given the potential well of the $\sim 10^{13}\ M_{\odot}$ SPT2349–56 halo (see below) constrained from the central velocity dispersion and radial distribution of cluster members (Miller et al. 2018; Hill et al. 2020). This is also a significant addition to the already abundant energy injection from the $6600\ M_{\odot}\ \text{yr}^{-1}$ of star formation being experienced by the core of SPT2349–56 from summing the SFRs of all member galaxies found in these works (Miller et al. 2018; Hill et al. 2020; Rotermund et al.

2021). We take the instantaneous injection of energy at $z = 4.3$ as

$$\dot{E}_{\text{kin}} = \frac{1}{2} \dot{M}_{\text{out}} v^2, \quad (7)$$

where \dot{M}_{out} is the total amount of gas ejected per unit time by galaxies and v is the outflow velocity. While v is not measured in SPT2349–56 galaxies, the average outflow in high- z SMGs and other star-forming galaxies has been constrained with increasingly large samples (e.g., Banerji et al. 2011; Förster Schreiber et al. 2014). We adopt a typical 500 km s^{-1} wind speed for the supernova-driven outflows in each SPT2349–56 galaxy. A mass outflow rate can then be found by converting SFRs into mass outflow rates \dot{M}_{out} by multiplying by a conservative mass loading factor $\eta = \dot{M}_{\text{out}}/\text{SFR} = 1$. η could even be greater than one based on observational (e.g., Newman et al. 2012) and theoretical work (e.g., Hopkins et al. 2012). However, the same amount of metals is found in stars and the ICM, which suggests equality, $\dot{M}_{\text{out}} \approx \text{SFR}$ (e.g., Renzini & Andreon 2014). We therefore obtain $\dot{E}_{\text{kin}} = (3.3 \pm 1.1) \times 10^{38} \text{ W}$, where the uncertainty reflects both the range in SFR estimates and the range of likely wind velocities. This energy injection is remarkably similar to that found from the radio-loud AGN above from Equation (6).

Estimating the total mechanical energy injected by the radio jets requires an estimate of the radio source lifetime. Brienza et al. (2017) and Hardcastle et al. (2019) have suggested that remnant sources fade rapidly, with most of the observed remnant radio galaxies being relatively young, with ages between 50 and 100 Myr.

With $\tau = 100 \text{ Myr}$ for SPT2349–56, we find $E_{\text{mech}} = P_{\text{cav}} \times \tau = (1.0 \pm 0.2) \times 10^{54} \text{ J}$, assuming only the uncertainty in the P_{cav} scaling relation.

4.1.2. Binding Energy of the Halo Gas

We then turn to estimating the binding energy of the gas in the SPT2349–56 halo. Giodini et al. (2010) demonstrated that the mechanical energy from jets is comparable to the binding energy (E_{binding}) in galaxy groups, while it is lower by a factor of 10^2 – 10^3 in clusters. Since the SPT2349–56 halo mass is comparable to a large group today, and the entire protocluster is expected to form a massive cluster by $z = 0$, it is thus of interest to investigate how E_{binding} compares to our estimate of E_{mech} .

We define the binding energy as the total potential energy needed to push the ICM gas within R_{500} (the radius where the mean dark matter halo density drops to 500 times the critical density) beyond R_{200} (the radius where the mean dark matter halo density drops to 200 times the critical density, which we assume to be equal to the virial radius). Hill et al. (2022) estimated M_{200} (the mass contained within R_{200}) to be $(9 \pm 5) \times 10^{12} M_{\odot}$, corresponding to $R_{200} = (120 \pm 70) \text{ kpc}$ at $z = 4.3$, and R_{500} can be computed if one assumes a density profile for the dark matter.

Following Giodini et al. (2010), the binding energy is computed as

$$\begin{aligned} E_{\text{binding}} &= \int_0^{M_{\text{gas},500}} [\phi(r) - \phi(R_{200})] dM_{\text{gas}} \\ &= 4 \pi \int_0^{R_{500}} \phi(r) \rho_{\text{gas}}(r) r^2 dr, \end{aligned} \quad (8)$$

where the constant term $\phi(R_{200})$ is small compared to the potential within R_{500} and can be ignored, and ρ_{gas} is the gas mass density.

Assuming the gas mass density follows the dark matter density but scaled by a single gas-mass fraction parameter, f_{gas} , we can adopt a Navarro–Frenk–White dark matter profile to write the binding energy as (see Giodini et al. 2010 for details)

$$E_{\text{binding}} = f_{\text{gas}} 4 \pi \rho_{\text{crit}} \delta_c A r_s^3 \int_0^{c_{500}} \frac{\ln(1+x)}{(1+x)^2} dx, \quad (9)$$

where $x = r/r_s$, with r_s being the characteristic radius related to the halo concentration parameter by $c = R_{200}/r_s$, δ_c is a numerical factor that depends only on the halo concentration parameter c , A scales with M_{200} and also depends on c , and ρ_{crit} is the critical density at the redshift of interest (here 4.3). We compute the concentration parameter using the mass-dependent relation of Macciò et al. (2007); they find a linear trend between $\log c$ and $\log M_{\text{vir}}$ (which we assume is equal to M_{200}), and we find $c = 7.9$, corresponding to $r_s = 15 \text{ kpc}$. We note that $c = 5$ is typically adopted for massive clusters $> 10^{14} M_{\odot}$. With the concentration parameter known, we calculate $R_{500} = 80 \text{ kpc}$ and $c_{500} = R_{500}/r_s = 5.3$.

At a redshift of 2.16, Tozzi et al. (2022a) were able to detect signs of a hot intracluster gas directly in the Spiderweb cluster using Chandra, through diffuse emission within a radius of 100 kpc not associated with the radio jets. They found it to be significantly softer than the central X-ray AGN and consistent with thermal bremsstrahlung from a hot ICM, implying a total mass of $3 \times 10^{13} M_{\odot}$.

We cannot estimate the halo gas mass directly in SPT2349–56, beyond summing the measured cold gas masses in individual galaxies from the core region and inferring additional cool and warm gas components in the halo. Summing the H_2 gas masses from the 23 SMGs within the cluster core from Hill et al. (2020) yields $M_{\text{gas,cool}} = 3 \times 10^{11} M_{\odot}$. The unseen gas components in the halo are more uncertain. A trend observed in groups and clusters is an increase of the fraction of hot gas with total system mass (Connor et al. 2014), approximately following $f_{\text{gas}} \propto M^{0.1-0.2}$, where $10^{13} M_{\odot}$ groups typically have f_{gas} of around 10%.

The L_X – M relation has been shown to remain approximately self-similar out to $z = 2$ (Mantz et al. 2018), including X-ray-detected clusters at $z = 2$ (Gobat et al. 2011). However, for low-mass systems the gas mass fractions may evolve with redshift (Connor et al. 2014). Regardless, this in itself does not constrain the ICM gas fraction, which requires more detailed X-ray properties than L_X to be detected.

Based on the above, we will assume for SPT2349–56 a gas mass of 10% of the halo mass, or $9 \times 10^{11} M_{\odot}$, which nominally requires that $M_{\text{gas,hot}} = 6 \times 10^{11} M_{\odot}$, unless there are substantial cold flows feeding the SMGs (Dekel et al. 2009). We estimate $E_{\text{binding}} = (1.5_{-1.4}^{+0.7}) \times 10^{54} \text{ J}$, where the uncertainty has been propagated from M_{200} and the uncertainty in the M_{200} – c scaling relation using a MCMC approach.

The radio feedback alone therefore conceivably provides all of the energy required to unbind the total gas in the cluster core. The stellar feedback has a comparable energy input, and could also be unbinding the cluster gas. However, the total energy is a minimum condition; the energy must also couple efficiently to the ICM. An energetic jet may not couple to the bulk of the

ICM gas (Babul et al. 2013; Yang & Reynolds 2016; Cielo et al. 2018).

Any hot ICM established at $z > 4$ may not be in hydrostatic equilibrium since cold inflows likely dominate the flow of gas in protocluster halos (Dekel et al. 2009). The infalling gas only increases the energy required to inflate a bubble in the nascent ICM, acting as an additive term to E_{binding} . While $L_{1.4}$ is fixed, the work done on an inflowing medium will be higher than for an ambient static medium. Therefore the $P_{\text{cav}} (\propto 4pV)$ to $L_{1.4}$ relationship might not hold when inflows dominate the halo. Yajima et al. (2022) and Trebitsch et al. (2021) have begun to explore some of these issues in hydrodynamical simulations of protoclusters, aiming to better understand AGN feedback and the impact of massive starburst galaxies in forming clusters. We leave more detailed calculations to future work.

4.1.3. Inferred X-Ray Luminosity and Accretion Rate

A correlation also exists between radio power and X-ray luminosity (L_X) for radio-loud AGNs (Ballo et al. 2012), although there is substantial scatter in this relation. While the correlation appears to be similar over a large range (nine orders of magnitude) in X-ray luminosity, there is a range of over 100 in L_X for a given radio luminosity in well-populated areas of the correlation. The relation plotted in Ballo et al. (2012) is characterized at 5 GHz rest frame, which we measure almost directly (through the ASKAP detection). Using the correlation, we find that $L_5 = 7 \times 10^{25} \text{ W Hz}^{-1}$ in the radio corresponds to $L_X = 10^{38} \text{ W}$ (where the X-ray luminosity is between 2 and 10 keV). We conclude that the X-ray emission from the central AGN in SPT2349–56 can be easily detected by XMM-Newton or Chandra under the full range of possible $L_X = 10^{37-39} \text{ W}$ suggested by this correlation. In the Spiderweb protocluster at $z = 2.16$, Tozzi et al. (2022a) used Chandra to detect X-ray emission in the radio jet regions, finding it well described by a power law with a spectral index of $\Gamma \sim 2-2.5$, and consistent with inverse-Compton upscattering of the cosmic microwave background photons by the relativistic electrons. Scheduled programs with XMM-Newton and Chandra will be able to elucidate the properties of SPT2349–56.

Finally, taking source C as the most likely host, we can infer the SMBH mass from the stellar mass that has been well characterized for C (Rotermund et al. 2021; Hill et al. 2022). For $M^* = 4 \times 10^{11} M_\odot$, the SMBH mass is $7 \times 10^8 M_\odot$ (e.g., Ding et al. 2020). From this, we can infer the range of Eddington luminosities with respect to the range in X-ray luminosity constrained by the radio power. In other words, how close to the maximal rate of accretion is the SPT2349–56 AGN if its SMBH is close to that implied by the stellar mass of source C. In particular, following Ballo et al. (2012), our measurements of $L_{5 \text{ GHz}}/M_{\text{BH}}$ constrain L_X/L_{Edd} to the range of roughly 0.005 to 0.05, based on their distribution shown (their Figure 10). Directly measuring the X-ray properties of SPT2349–56 will allow substantial progress in characterizing the system and its environment.

4.2. Implications of the Steep Spectrum

For an optically thin synchrotron source, the spectrum will steepen in spectral index from low to high frequencies by $\Delta\alpha = -0.5$ if the source lifetime is greater than the timescale for energy loss from the radiating electrons. This leads to a concave spectral shape with a characteristic bend frequency, ν_b

(Kellermann et al. 1969). Thus the age of the electron population within radio jets contributes to the steepness of the spectrum. Three effects will then decrease ν_b as the source redshift increases (Krolik & Chen 1991): (i) for a fixed bend frequency ν_* in the rest frame, the observed bend $\nu_b = \nu_*/(1+z)$; (ii) losses due to inverse-Compton scattering off the microwave background rise with redshift as $(1+z)^4$, so that for a fixed time electrons spend in the radiating region, the lowest-energy electron that can cool has a frequency (or energy), which decreases with increasing redshift; and (iii) flux-limited samples result in a selection effect that favors low ν_* at high- z . Sources must have higher emissivity at higher redshift to be included in the sample. They also must have stronger implied magnetic fields, and therefore more rapid synchrotron losses.

A combination of these effects has been used to explain the observed trend that higher-redshift radio galaxies have steeper spectral indices (van Breukelen et al. 2009; Carilli & Walter 2013). The ultra-steep spectral indices of HzRGs (up to the $\alpha = 1.6$ we find in SPT2349–56) is a main selection criterion for identifying these powerful radio sources in the distant Universe (De Breuck et al. 2000; Broderick et al. 2007). All three HzRGs shown in Figure 2 in fact have α very close to 1.6. It is of note that SPT2349–56 would have been discovered by these HzRG surveys over one to two decades ago had the radio source been 10–100 times more radio luminous, and even cursory submm follow-up would then have revealed the extended $S_{850} = 110 \text{ mJy}$ source that belies its nature as a submm-luminous protocluster.

A steep spectrum generally argues for self-absorbed synchrotron and a lack of electron injection (e.g., Radcliffe et al. 2021). Thus the steep α in SPT2349–56 could represent a dying radio source. In this case, the ATCA flux should be extended over the same area as the ASKAP data, and SPT2349–56 could be a young and completely unresolved compact radio source. On the other hand, this might be a “contained” or “frustrated” radio source inside a dense medium, sometimes referred to as a compact steep spectrum (CSS) source (Padovani 2017), but an issue with this interpretation is that the luminosity of the source is low relative to these typical GHz-peaked sources. If self-absorbed synchrotron is contributing to the steep spectrum, the observational constraints would mean that the break frequency is well below about 5 GHz in the rest frame. In principle, this break frequency can provide a constraint on the age of the radio source, but since we do not constrain this break with the current data we do not pursue this further here. However, if the radio emission is due to a CSS then it would have to be older than 500 Myr to have a break frequency below 0.9 GHz (4.8 GHz rest; Padovani 2017).

4.3. Connection to the Ly α blobs

The powering sources of LABs have often been identified broadly with the photoionizing emission from a close ionizing source (e.g., a QSO; Geach et al. 2009; Overzier et al. 2013), shocks (e.g., Taniguchi & Shioya 2000), or “cooling radiation” during gravitational collapse of the gas (e.g., Haiman et al. 2000). The SPT2349–56 LAB (shown in Figure 7) was originally hypothesized to be heated by some combination of the three ALMA sources that reside near or within it (Apostolovski et al. 2023). However, given that the LAB center is only $4''.5$ (31 kpc in projection) offset from ALMA source C, it could instead be heated by the radio-loud AGN.

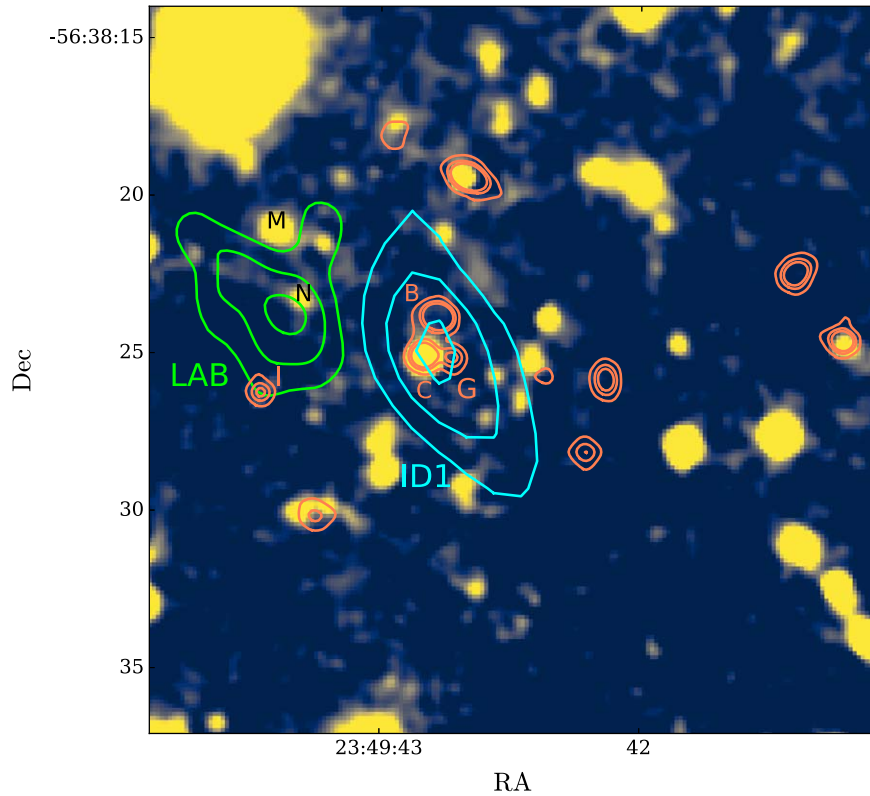


Figure 7. Does the radio-loud AGN power the LAB? The background shows HST F160W imaging with ATCA 2.2 GHz contours (cyan) and the Apostolovski et al. (2023) MUSE Ly α contours (lime). The center of the LAB lies $4''.5$ (31 kpc) from the radio source centroid. ALMA 850 μm contours are shown (coral), but sources M and N are too weak to see in this representation. The LAB is centered near the SMG, N, which was originally identified through its [C II] emission and undetected in continuum (Miller et al. 2018). N has $S_{1.1\text{ mm}} = 0.18\text{ mJy}$ and an $L_{\text{IR}} = 4 \times 10^{11} L_{\odot}$, with an implied SFR = $35 M_{\odot} \text{ yr}^{-1}$.

The LAB is centered on the weak SMG, N, which was originally identified through its [C II] emission (Miller et al. 2018). N is a luminous infrared galaxy (LIRG) with $S_{850} = 0.27 \pm 0.04\text{ mJy}$, $L_{\text{FIR}} = 4 \times 10^{11} L_{\odot}$, and a substantial $\dot{M}^* = 3 \times 10^{10} M_{\odot}$. It is a plausible, though somewhat unlikely, power source for the luminous LAB (whose total luminosity is $3 \times 10^{42}\text{ erg s}^{-1}$, or $3 \times 10^{35}\text{ W}$); source N fails to provide the necessary UV ionizing photons by at least a factor of 10, scaling from its meager R-band flux density of $0.37\text{ }\mu\text{Jy}$ (similar to the analysis in Apostolovski et al. 2023). We can directly estimate the AGN X-ray emission expected for powering the LAB following Overzier et al. (2013), assuming that the fraction of ionizing photons that will cascade to Ly α is 68% (case B recombination). This number likely exceeds the actual amount of ionizing radiation available due to the absorption by dust by a factor of around 10, which we account for here. We then assume a radio-quiet QSO spectrum given by Richards et al. (2006). The predicted observed frame (0.2–12 keV) X-ray luminosity would be $2 \times 10^{37}\text{ W}$, which is comparable to the low end of the expected range of L_{X} from the SPT2349–56 radio source, as discussed above. The radio AGN may therefore be at least as plausible a heating source as N.

Regarding the LAB being spatially offset from the AGN position, we note that in the radio source B3 J2330 at $z = 3.1$ (Matsuda et al. 2009), the peak of the Ly α emission was also found to be similarly offset from the HzRG itself. Even in the $z = 4$ Distant Red Core (DRC) LAB, there is a roughly $3''$ (21 kpc) offset from the X-ray-emitting AGN that is proposed as the LAB’s power source (Vito et al. 2020). However, these

are rare cases. Venemans et al. (2007) showed that generally the AGN is very near the center of the Ly α halo, which grants some geometrical credence to the idea that the Ly α halo is ionized by the central AGN’s photons. In SPT2349–56, this is harder to argue, but the Ly α could be completely absorbed by the copious amounts of dust in the core. The SPT preselection (as with the Herschel selection of the DRC) may favor finding sources with such offsets.

4.4. AGN Fractions in Protoclusters

As described in Section 3.1, with $27\text{ }\mu\text{Jy}$ rms at 2.2 GHz, we are sensitive to moderately luminous and heavily obscured $z = 4.3$ AGNs among the 30 SMGs identified in the SPT2349–56 structure. They need to lie approximately 5 times above the radio–FIR relation to be significantly (5σ) detected by ATCA. In GOODS-N (Figure 3), there are seven radio sources (all lacking submm detection) that satisfy this threshold, all of which lie at redshifts less than 2. Another seven such radio sources lie 2–3.5 times above the relation, extending to a redshift of about 4, which would not be detected by our observations. The fact that all submm-detected sources in GOODS-N and 74 of 76 SMGs in ALESS are consistent with the radio–FIR relation does signify that radio-loud AGN are not common among the submm-luminous population. No significant radio emission is found from any other (non-SMG) cluster members or candidates. With our current radio depth, the radio-AGN content among SMGs in this protocluster is constrained to be less than 10% (three of 30 members), and most likely 3% (assuming C is the host of the ATCA radio source). However, the radio-loud AGNs are only about 10% of the total AGN

population in the field (Barger et al. 2007; Radcliffe et al. 2021). The X-ray AGN fraction remains unconstrained, and given that many X-ray AGNs are not radio emitters (Barger et al. 2007), our AGN fraction estimates in SPT2349–56 are lower limits.

In the $z = 4.0$ DRC protocluster (Oteo et al. 2018), a central galaxy is radio undetected, but is a Compton-thick X-ray AGN. Only one of the three X-ray-identified AGNs is detected in the radio, DRC6 ($S_{5.5} = 128 \mu\text{Jy}$, $S_9 = 120 \mu\text{Jy}$), indicating a flat-spectrum source. In this case, the radio AGN in the DRC lies toward the edge of the projected distribution of SMGs (offset from the core of the cluster). Thus without X-ray data, we cannot tell if the total AGN fraction of SPT2349–56 is different from that in the DRC (23%; Vito et al. 2020). As another example, in the core of the $z = 3.09$ SSA22 protocluster, the SMGs have a 50% X-ray AGN fraction, with four of eight SMGs detected by Chandra (Umehata et al. 2019), significantly larger than the DRC.

4.5. Radio Sources and Cluster Evolution

Given that SPT2349–56 is conceivably the most massive and active halo we know of at $z > 4$, an open question concerns the feedback or radio mode that this AGN is operating in, and how it is shaping the early core evolution of the cluster. With the current data, having only the two photometric points characterizing the radio emission and not even localizing it uniquely to one galaxy, we cannot definitively address these issues. Most radio-loud AGNs appear to be hosted in recent or ongoing mergers (e.g., Ramos Almeida et al. 2012; Chiaberge et al. 2015). In this light, it may not be too surprising to find a radio-loud AGN in the core of SPT2349–56. Given that the radio luminosity of SPT2349–56 is modest for an HzRG, we may be seeing a radio-loud AGN fueled via radiatively inefficient flows with low accretion rates (Best & Heckman 2012). In this picture, the gas supplying the radio galaxy is frequently associated with hot X-ray halos surrounding massive galaxies, groups and clusters, as part of a radio-AGN feedback loop. This contrasts with more luminous radio sources (e.g., TNJ1338) thought to be fueled at higher rates through radiatively efficient standard accretion disks by cold gas (Best & Heckman 2012). These more luminous radio sources are hypothesized to have fuel brought in through mergers and interactions, which are in fact abundant in SPT2349–56. The debate thus remains open as to whether we are seeing a decaying radio source or a radio source quickly building in luminosity. By better specifying the radio emission and its origin, we could learn about the buildup and state of the ICM that may already be present at $z = 4.3$.

5. Conclusions

We have presented ATCA radio observations of SPT2349–56, a starbursting and gas-rich protocluster, consisting of over 30 SMGs at $z = 4.3$. We placed SPT2349–56 in context with microjansky radio sources in the GOODS-N and ALESS fields, and with the other 22 gravitationally lensed SPT-SMGs also observed with ATCA in our program. We also studied in detail the central galaxies identified by ALMA in SPT2349–56 near this strong radio detection.

1. We detected a single source at 2.2 GHz in SPT2349–56, spatially coincident with the central three luminous members of the protocluster, denoted B, C, and G in

Miller et al. (2018). While the ATCA and MeerKAT radio centroid lies close to source C, which has the largest stellar mass in the protocluster, we cannot rule out that the radio emission is coming from B or G, or even a combination of the galaxies.

2. Under any of the possibilities above, the $214 \mu\text{Jy}$ flux density at 2.2 GHz translates to more than 20 times the radio luminosity expected from the FIR–radio correlation defined by star-forming galaxies, and suggests that an AGN is driving the radio emission.
3. The radio source has a steep spectrum, with an index of $\alpha = -1.45 \pm 0.16$, constrained by the MeerKAT 816 MHz and ASKAP 888 MHz detections, and the ATCA nondetections at 5.5 and 9 GHz, consistent with an AGN.
4. No other clear signs of AGN activity have yet been detected in this protocluster using any other diagnostics available to us (CO SLEDs; $\text{EW}(\text{OH}_{163\mu\text{m}})$, $[\text{C II}]/\text{FIR}$ ratios; optical spectra), highlighting the radio continuum as a powerful probe of obscured AGNs in high- z protoclusters.
5. The three SMGs likely associated to the radio source have among the highest gas and dynamical mass of the protocluster members (Rotermund et al. 2021). Moreover, high-resolution ALMA imaging resolves this system into multiple interacting, star-forming clumps, with a surrounding arc of $[\text{C II}]$ emission (Hill et al. 2020; N. Sulzhanauer et al. 2023, in preparation). This is consistent with the idea that the availability of large amounts of gas and galaxy interactions, both of which are enhanced in gas-rich overdensities at high redshift, can trigger fast and obscured SMBH accretion.
6. No significant radio emission (nor any other robust AGN signature) is found from any other cluster member, constraining the radio-loud AGN content among SMGs in this protocluster to no more than 10% (three of 30 members), and likely just 3%. A radio-stacking analysis on the remaining 10 brightest SPT2349–56 SMGs finds $(11 \pm 10) \mu\text{Jy}$, which is consistent with the average 2.2 GHz emission from star formation via the FIR–radio correlation. We thus find no evidence that nuclear accretion powering radio emission exists below our detection threshold in other SMG members of SPT2349–56. However, radio-loud AGNs represent only 10% of all AGNs, and X-ray observations and JWST IR spectroscopy would be the next key steps to constrain AGNs in this system and compare to AGN fractions found in other protoclusters.
7. The SPT2349–56 radio-loud AGN has a luminosity density of $L_{2.2} = 4.4 \times 10^{25} \text{ W Hz}^{-1}$, extrapolating to $L_{1.4,\text{rest}} = (2.2 \pm 0.2) \times 10^{26} \text{ W Hz}^{-1}$ with the measured $\alpha = -1.45$, which is still over two orders of magnitude less luminous than the powerful radio galaxies normally studied at these redshifts. Many such HzRGs have rich protocluster environments; however, it remains unclear if the opposite is true, that all massive $z > 4$ protoclusters have a central radio galaxy.
8. The fact that the radio AGN is detected in the hypothesized central seed of a growing BCG galaxy with significant stellar mass already in place makes this discovery an important new ingredient in understanding the formation and evolution of the cluster.

9. The radio luminosity was used to infer a radio jet power of $P_{\text{cav}} = (3.3 \pm 0.7) \times 10^{38}$ W, sufficiently large as to provide a dominant feedback on the cooling gas in the $10^{13} M_{\odot}$ halo. The radio luminosity also suggests a strong X-ray source with $L_X = 10^{38}$ W (integrated between 2 and 10 keV), easily detectable by Chandra or XMM-Newton. SPT2349–56 therefore has a high-luminosity AGN, even if in the form of a highly obscured quasar, and JWST will be a powerful tool to uncover its properties through high-ionization IR emission lines.

Acknowledgments

The Australia Telescope Compact Array is part of the Australia Telescope National Facility (<https://ror.org/05qajvd42>), which is funded by the Australian Government for operation as a National Facility managed by CSIRO. This paper includes archived data obtained through the CSIRO ASKAP Science Data Archive, CASDA (<http://data.csiro.au>). The MeerKAT telescope is operated by the South African Radio Astronomy Observatory, which is a facility of the National Research Foundation, an agency of the Department of Science and Innovation. The research of R. P.D. is supported by the South African Research Chairs Initiative (grant ID 77948) of the Department of Science and Innovation and National Research Foundation. The Australian SKA Pathfinder is part of the Australia Telescope National Facility (<https://ror.org/05qajvd42>), which is managed by CSIRO. Operation of ASKAP is funded by the Australian Government with support from the National Collaborative Research Infrastructure Strategy. ASKAP uses the resources of the Pawsey Supercomputing Centre. The establishment of ASKAP, the Murchison Radio-astronomy Observatory, and the Pawsey Supercomputing Center are initiatives of the Australian Government, with support from the Government of Western Australia and the Science and Industry Endowment Fund. We acknowledge the Wajarri Yamatji people as the traditional owners of the Observatory site. The National Radio Astronomy Observatory is a

facility of the National Science Foundation operated under cooperative agreement by Associated Universities, Inc. This paper makes use of the following ALMA data: ADS/JAO.ALMA#2015.1.01543.T, ADS/JAO.ALMA#2018.1.00058.S, and ADS/JAO.ALMA#2021.1.01010.P. ALMA is a partnership of ESO (representing its member states), NSF (USA) and NINS (Japan), together with NRC (Canada), MOST and ASIAA (Taiwan), and KASI (Republic of Korea), in cooperation with the Republic of Chile. The Joint ALMA Observatory is operated by ESO, AUI/NRAO and NAOJ. S.C., A.B., and D.S. gratefully acknowledge support for this research from NSERC. M.A. acknowledges support from FONDECYT grant No. 1211951, CONICYT + PCI + INSTITUTO MAX PLANCK DE ASTRONOMIA MPG190030. M.A. and M.S. acknowledge support from CONICYT + PCI + REDES 190194 and ANID BASAL project FB210003. K.A.P. and M.A. are supported by the Center for AstroPhysical Surveys at the National Center for Supercomputing Applications as an Illinois Survey Science Graduate Fellow.

Appendix A

In this appendix, we further assess the offsets between source centroids in the 888 MHz ASKAP image and the ATCA 2 GHz (and MeerKAT 816 MHz) image that were discussed in Section 3.1 (Figure 8). We measured peak fluxes in both images for all sources within a $13'$ radius of SPT2349–56, measured their centroids, and calculated radial offsets for each. The offsets appear random in orientation, with the mean x and y offset being close to zero ($0''.3, -0''.2$). In Figure 8, we plot the radial offsets versus ASKAP flux. SPT2349–56 shows the largest offset, which could indicate that its origin may be physical. It has a 4.6σ deviation from the median (excluding SPT2349–56) offset of $1''.4$. Even restricting the analysis to those sources with comparable flux densities and S/Ns ($S_{888} < 2$ mJy) only increases the median offset to $1''.6$.

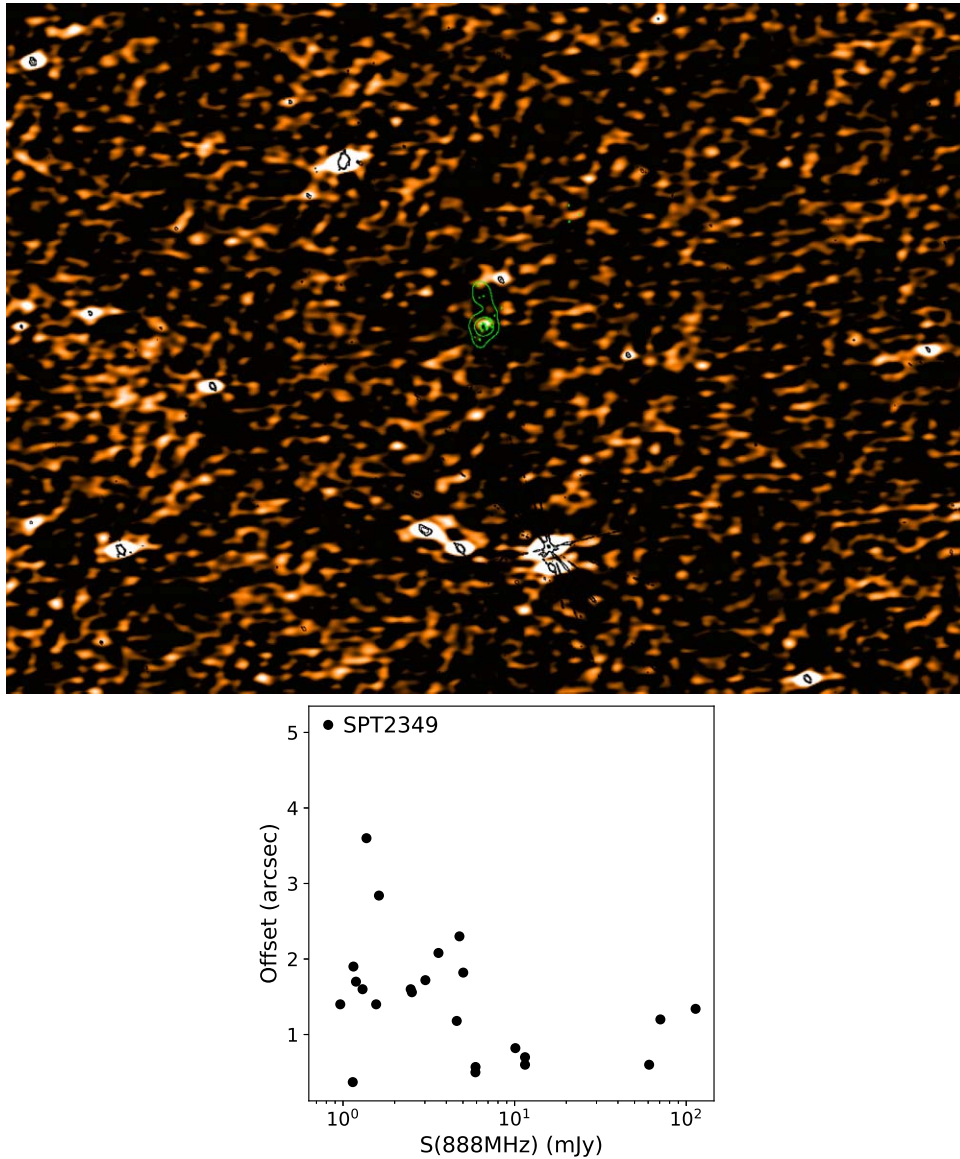


Figure 8. Assessing the offsets between ASKAP and ATCA sources. Top: the 888 MHz ASKAP image surrounding SPT2349–56 (green LABOCA contours, showing ALMA sources as green dots) with ATCA 2 GHz contours overlaid ($26' \times 19'$ field shown). Bottom: the radial offsets between the centroids for sources common in both images. SPT2349–56 shows the largest offset, which might therefore require a physical interpretation. It has a 4.6σ deviation from the median (excluding SPT2349–56) offset of $1''.4$ offset.

Appendix B

In this appendix and Figures 9–11, we show the CO $J=7$, 11, and 16 lines for the central B, C, and G sources, whose line strengths are plotted in the SLED diagram (Figure 5). We also show the H₂O lines that are used to compare with the FIR luminosity estimates from Hill et al. (2020).

In order to measure line strengths, the bright and well-detected [C II] lines provided in Hill et al. (2020) were used as a template. These [C II] lines were fit by single- and double-Gaussian profiles, and we selected the integration range by scaling the [C II] profile to the rest frequency of the line of interest and then summing channels between -2σ and 2σ (where σ is the standard deviation of the best-fitting line width), or for cases where two Gaussians were a better fit, from $-2\sigma_L$ to $+2\sigma_R$, where σ_L and σ_R are from the left and right Gaussian fits, respectively.

The CO(7–6) line is blended with the [C I](2–1) line, and the CO(16–15) line is blended with the OH doublet, so these had to be fit and subtracted before integrating over the CO lines. For the former case, where both CO(7–6) and [C I](2–1) are both well detected in B and C, we simultaneously fit single-Gaussian profiles at the locations of the two lines, then subtract the best-fit [C I](2–1) model from the spectrum and sum over the relevant channels as described above (then vice versa to obtain [C I](2–1) line strengths). For source G, we do not see any strong line features around the expected [C I](2–1) frequency, so we simply sum over the CO(7–6) and [C I](2–1) channels in the raw spectrum. The CO(16–15) line is not well detected for any sources but the OH doublet is, so we fit a Gaussian to these OH lines and subtract the models before summing over the CO(16–15) channels. In the fit we force the amplitude of each doublet component to be equal, and we fix the width of each doublet component to be equal to the width of the [C II] line (described in Section 3.3; see Table 4). Since the profile for G

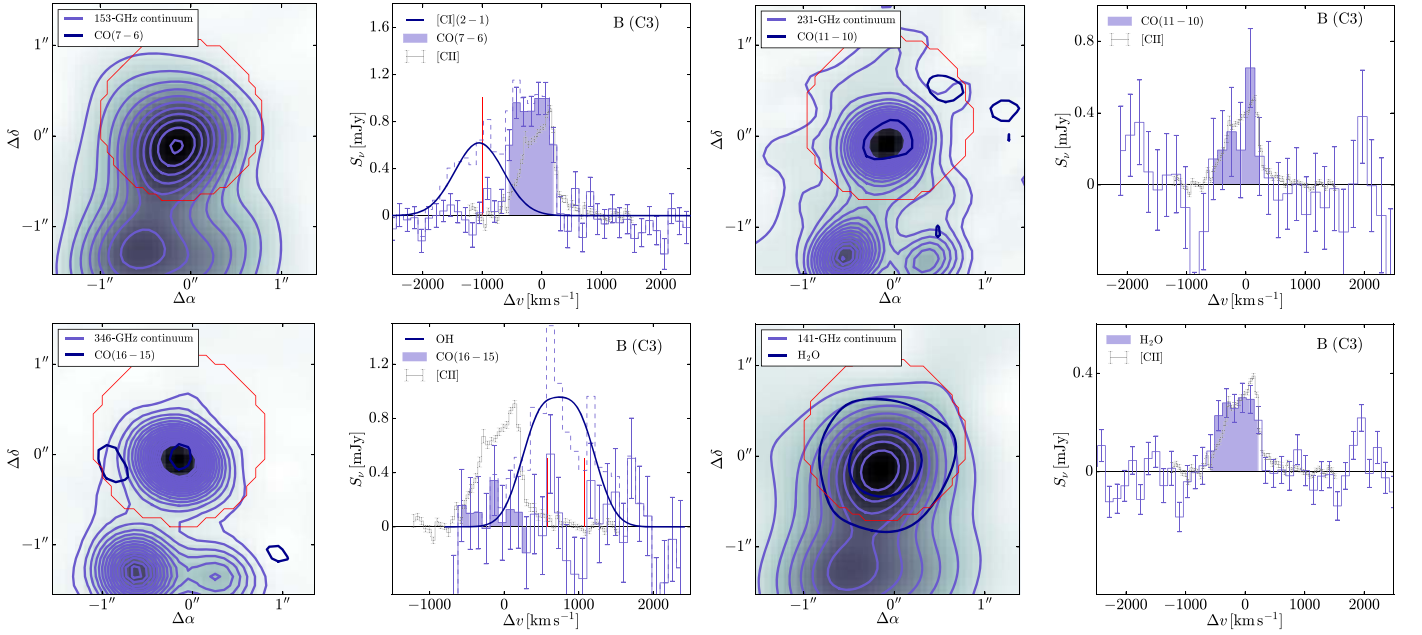


Figure 9. Cutouts and spectra of CO(7–6), CO(11–10), CO(16–15), and H₂O line emission for galaxy B. The cutouts in each panel show continuum emission (obtained by averaging over all line-free channels) and line emission (obtained by averaging over all channels where the line is expected; see Section 2 for details), with contours starting at 2σ and increasing in steps of 3σ . Apertures are shown as red circles, and used to obtain the spectra shown in the right panels. In each spectrum plot, we show the [C II] profiles from Hill et al. (2020), scaled to the expected frequency of the given line, and arbitrarily normalized. The shaded regions show the integration ranges (set to be $\pm 2\sigma$ about the [C II] line; see Section 2) used to obtain line strengths. The CO(7–6) line is blended with the [C I](2–1) line, and the expected central frequency (or for G, two central frequencies as the [C II] profile has two components) of the [C I](2–1) is marked in red. The [C I](2–1) line is fit by a Gaussian profile and subtracted, and the original spectra are shown by the dashed lines. Similarly, the CO(16–15) line is blended with the OH doublet, and we mark the mean frequency of each OH line in red (corresponding to two frequencies for B and C, and four frequencies for G). The OH doublet is fit by a scaled [C II] profile (see Section 2) and subtracted, and the original spectra are shown by the dashed lines.

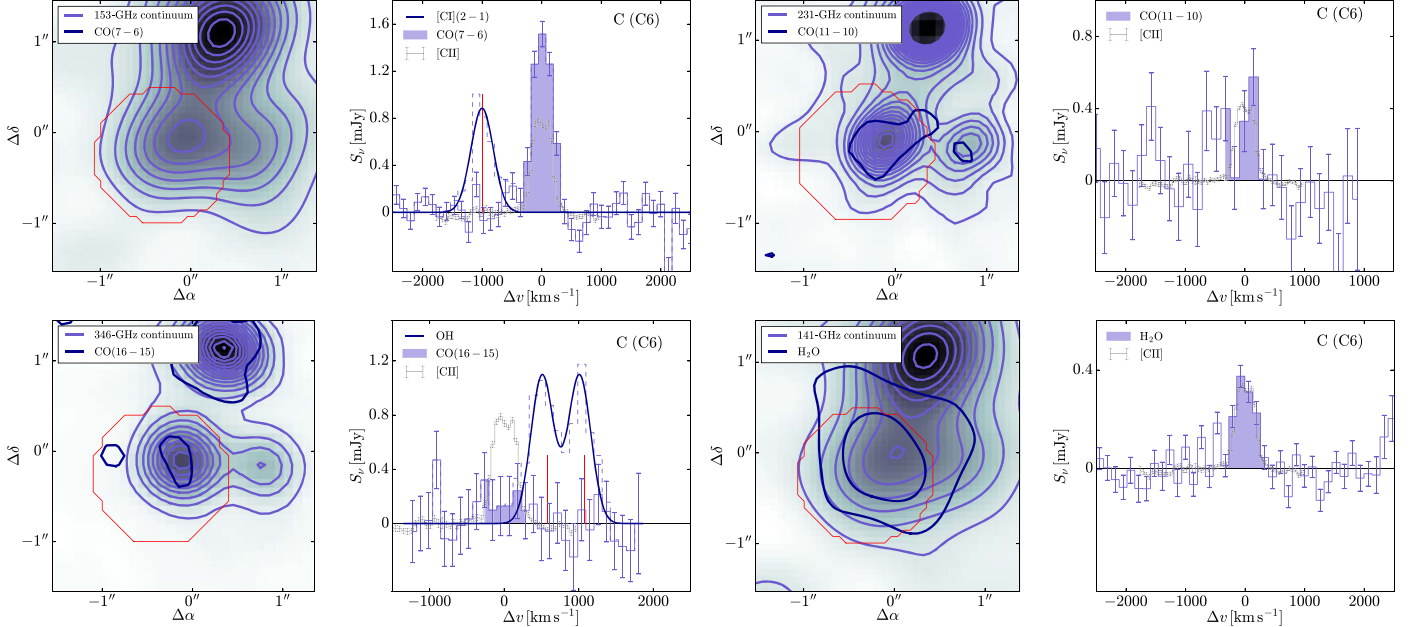


Figure 10. Same as Figure 9 but for galaxy C.

is two Gaussians, we include an additional OH doublet component of equal amplitude and fixed frequency separation/width to match the [C II] profile. This leaves two free parameters in all fits: the frequency of the first doublet, and the amplitude of all the components. In Figure 9, we can see that for source B the two OH doublet components are blended with

each other due to the large FWHM of the system, and for G the four components blend into three peaks.

Lastly, Band 4 and Band 6 continuum flux densities were estimated by averaging over all line-free channels in the original (non-continuum-subtracted) data cubes (again using the [C II] line as a template). We combined channels from the

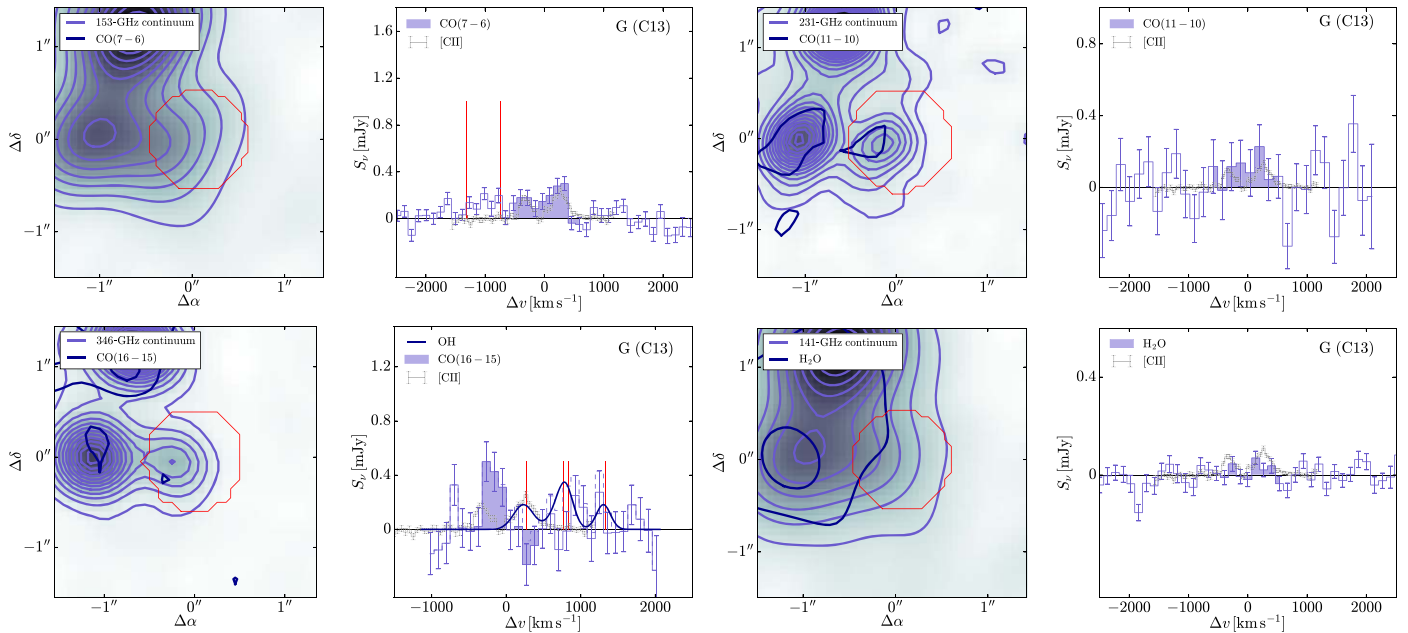


Figure 11. Same as Figure 9 but for galaxy G.

lower and upper sidebands of these observations, meaning they are at observed frequencies of 147 and 231 GHz, respectively. Band 7 continuum flux densities (around the CO(16–15) and OH lines) are already provided in Hill et al. (2020).

Appendix C

Here, we describe the ATCA observations of the full sample of 23 SPT-SMGs observed in the survey program, shown in Figure 3. These SPT-SMGs were drawn from the complete sample of 81 sources (Reuter et al. 2020), selecting those that had the best redshift constraints at the time of observations. All but three of the 23 SPT-SMGs are detected at $>4\sigma$ significance at 2.2 GHz. The 2.2 GHz flux densities are measured at peak pixels (Table 5), as in all cases the sources are unresolved in the $8'' \times 5''$ beam. The restored beam sizes and PAs are also listed in Table 5. ALMA 850 μm overlays are shown in Figure 12 (data from Spilker et al. 2016 and Reuter et al. 2020). LABOCA 850 μm fluxes and ALMA-derived redshifts from Reuter et al. (2020) are also listed in Table 5 for completeness.

Most sources are not detected or only marginally detected at 5.5 GHz (nine detections at $>3\sigma$) and 9.0 GHz (four detections at $>3\sigma$). For those sources detected at these higher frequencies with ATCA, we measure flux densities from peak pixels when the source is unresolved or as aperture measurements when the source is resolved. We show the nine sources detected at 5.5 GHz in Figure 13, and the four sources detected at 9.0 GHz in Figure 14. We have also searched for detections in the ASKAP 0.888 MHz RACS survey described in Section 2.2, listing their flux densities in Table 5. We find 15 of the 23 sources are significantly detected by ASKAP.

We derive radio spectral indices directly for all sources with at least two radio detections, and list these together with flux densities in Table 5. The data were fit according to a linear function using a MCMC algorithm implemented by the `emcee` package (Foreman-Mackey et al. 2013). This MCMC package samples the posterior probability function, and is used to determine the error contours shown in Figure 2, as well as the

uncertainties on α in Table 5. We summarize their radio spectral indices in Figure 15 and Table 5.

The lensed SMGs are shown in Figure 3, where we estimate their rest 1.4 GHz luminosities directly using the measured α , or with $\alpha = -0.8$ if only detected at a single radio frequency. In general these SPT-SMGs follow the same FIR–radio correlation as the other field samples shown. However, three sources are highly significant outliers from the FIR–radio correlation: SPT0125–50 at $z = 3.96$, SPT0202–61 at $z = 5.02$, and SPT0550–53 at $z = 3.13$. Given how rare such strong outliers are in the field SMG samples (only one of 76 SMGs shows anywhere near this level of radio excess in the ALESS SMG sample; Thomson et al. 2014), we propose that the lensing galaxy rather than SMG may be the more likely radio AGN in these three cases. These radio-excess sources exhibit steeper radio indices than typical star-forming galaxies, comparable to or exceeding SPT2349–56. Without knowing if the lens or source redshift is correct, we cannot reasonably apply the radio K -correction to estimate the rest 1.4 GHz luminosity, and therefore we do not include these three in Figure 3.

In particular, SPT0550–53 shows an extended radio morphology/jet, well resolved in all three ATCA frequencies, which is more naturally explained by a lower-redshift, radio-loud galaxy. Further, the optical spectrum of the lens SPT0550–53 shows AGN emission lines. Neither SPT0125–50 nor SPT0202–62 show AGN signatures in their optical spectra. SPT0125–50 is curious as the ATCA 2 GHz flux density is very close to that expected from the FIR–radio relation, however ASKAP reveals a 3 mJy source well centered on SPT0125–50, implying an incredibly steep $\alpha = -2.24$. Thus any K -correction to lower rest-frame frequencies than that probed by 2.2 GHz observations quickly places SPT0125–50 significantly above the FIR–radio correlation.

These results also raise the question of whether the radio emission in other lensed SPT-SMGs might be contaminated from the often massive lens galaxy (Rotermund 2020). While in some examples, especially in SPT0538–50, the radio

Table 5
ATCA Observations at 2.2, 5.5, and 9.0 GHz, as Well as ASKAP at 888 MHz, of 23 SPT-SMGs

Name	t_{int} (hr)	$S_{2.2}$ (μJy)	Beam ^a ($'' \times ''$)	PA ^b (deg)	$S_{5.5}$ ^c (μJy)	$S_{9.0}$ ^c (μJy)	$S_{0.9}$ ^f (μJy)	S_{850} (mJy)	z	α ^c	Comment ^g
SPT 0027–50	0.58	334 ± 31	8×4	106	<105	<150	1064 ± 201	48	3.444	-1.28 ± 0.25	n n
SPT 0103–45	0.54	229 ± 29	8×4	16	<111	<159	<589	125	3.092	...	n n
SPT 0109–47	0.56	1106 ± 31	9×5	11	824 ± 36	461 ± 52	1417 ± 194	109	3.614	-0.42 ± 0.04	yR yR
SPT 0125–47	0.59	586 ± 35	9×5	112	382 ± 36	193 ± 49	1835 ± 201	144	2.515	-0.82 ± 0.10	y mR
SPT 0125–50	0.56	365 ± 29	5×7	110	<102	<156	2792 ± 194	109	3.959	-2.25 ± 0.12	n n
SPT 0202–61	0.68	710 ± 35	9×5	6	225 ± 40	<153	1943 ± 179	109	5.018	-1.16 ± 0.09	y n
SPT 0245–63	0.71	94 ± 33	9×4	77	<99	<135	<598	61	5.626	...	n n
SPT 0345–47	0.68	275 ± 29	8×6	174	<99	<132	701 ± 194	89	4.296	-1.03 ± 0.38	n n
SPT 0346–52	0.72	162 ± 38	5×9	68	<105	<132	<603	131	5.656	...	n n
SPT 0418–47	0.70	173 ± 22	8×5	163	<93	<135	430 ± 198	108	4.224	-0.99 ± 0.67	n n
SPT 0512–59	0.56	465 ± 34	7×5	153	<177	<231	1531 ± 197	75	2.233	-1.32 ± 0.17	n n
SPT 0529–54	0.54	260 ± 50	8×5	153	<120	<180	<586	118	3.369	...	n n
SPT 0532–50	0.57	489 ± 39	8×5	154	144 ± 49	<177	1093 ± 231	118	3.399	-1.06 ± 0.16	m n
SPT 0538–50	0.56	581 ± 36	8×5	157	341 ± 59	168 ± 58	1490 ± 237	125	2.786	-0.81 ± 0.13	yR mR
SPT 0550–53	0.55	1288 ± 48	9×6	169	446 ± 39	270 ± 56	4060 ± 187	53	3.128	-1.22 ± 0.05	yR yR
SPT 0551–50	0.56	286 ± 25	8×6	160	159 ± 45	<171	520 ± 185	74	3.164	-0.70 ± 0.24	m n
SPT 2031–51	0.48	269 ± 31	9×5	51	<123	<186	721 ± 203	65	2.452	-1.08 ± 0.39	n n
SPT 2134–50	0.53	334 ± 47	8×4	33	174 ± 43	<162	804 ± 196	101	2.780	-0.90 ± 0.44	y n
SPT 2319–55	0.54	75 ± 44	8×4	47	<126	<174	<600	38	5.293	...	n n
SPT 2332–53	0.56	244 ± 23	9×5	36	146 ± 41	<162	<581	57	2.756	-0.82 ± 0.56	m n
SPT 2349–56	0.56	215 ± 27	8×4	30	<120	<162	867 ± 189	106 ^d	4.303	-1.45 ± 0.16	n n
SPT 2353–50	0.56	24 ± 53	9×5	30	<138	<159	<594	41	5.576	...	n n
SPT 2357–51	0.55	131 ± 19	9×5	31	<108	<156	<589	53	3.070	...	n n

Notes. We also include unresolved LABOCA 850 μm flux densities (S_{850}), ALMA redshifts, and best-fit spectral indices.

^a The 2.2 GHz beam is quoted as x and y FWHM. The 5.5 GHz beam is typically $3''6 \times 2''2$. The 9.0 GHz beam is typically $2''2 \times 1''2$.

^b The PA of the 2.2 GHz beam is the angle east of north.

^c The radio spectral index α , defined as $S_\nu \propto \nu^\alpha$.

^d In SPT2349–56 we have assumed source C with $S_{850\mu\text{m}} = 4.7$ mJy is the host of the AGN, although it could be B or G as described in the text; here we still provide the unresolved LABOCA flux density.

^e At 5.5 and 9.0 GHz, the 3σ upper limit is listed unless there is a detection at $>3\sigma$ at the ALMA position.

^f The 888 MHz measurements are from the ASKAP RACS survey, described in Section 2.2. Sources with $<3\sigma$ positive signal are listed at these limits.

^g Comments list whether 5.5 GHz and 9.0 GHz data show detections $>4\sigma$ (y), marginal detections (m) where $<4\sigma$ flux density is measured at the ALMA position, or no detection (n). We indicate the four sources with resolved radio morphologies (R), in SPT0538–50 clearly following the ALMA emission, although in SPT0109–47 and especially SPT0550–53 the resolved emission appears to be an extended lobe or jet.

emission is directly identified as coming from the ALMA-detected lensed SMG components, in others the Einstein radius of the lensed source (Spilker et al. 2016) is too small to be detected offset from the lens galaxy itself, even at 9 GHz. The distribution in α constrained by the fits in Figure 15 show a mean of -0.93 ± 0.14 , offset steeper, but still consistent with, the $\alpha = -0.8$ found in samples of unlensed SMGs reported in Section 3.2 (e.g., Thomson et al. 2014). Several of the higher-redshift sources in Figure 3 do in fact show a marginal excess over that expected from the FIR–radio correlation. This excess sometimes appears only due to the

comparison shown at rest 1.4 GHz, accentuating the K -correction from their steeper than average α we measure. Given the large uncertainties from the often two-point α estimates, this may be inconsequential. Generally, optically identified AGNs are relatively rare in the *distant red galaxies* that are often found to lens these SMGs (Rotermund 2020), and the gravitationally boosted radio signal associated with the high-SFR SMG is a more probable source of the strong radio emission we see in these 19 SPT-SMGs. Their radio emission is not obviously contaminated by their foreground lens.

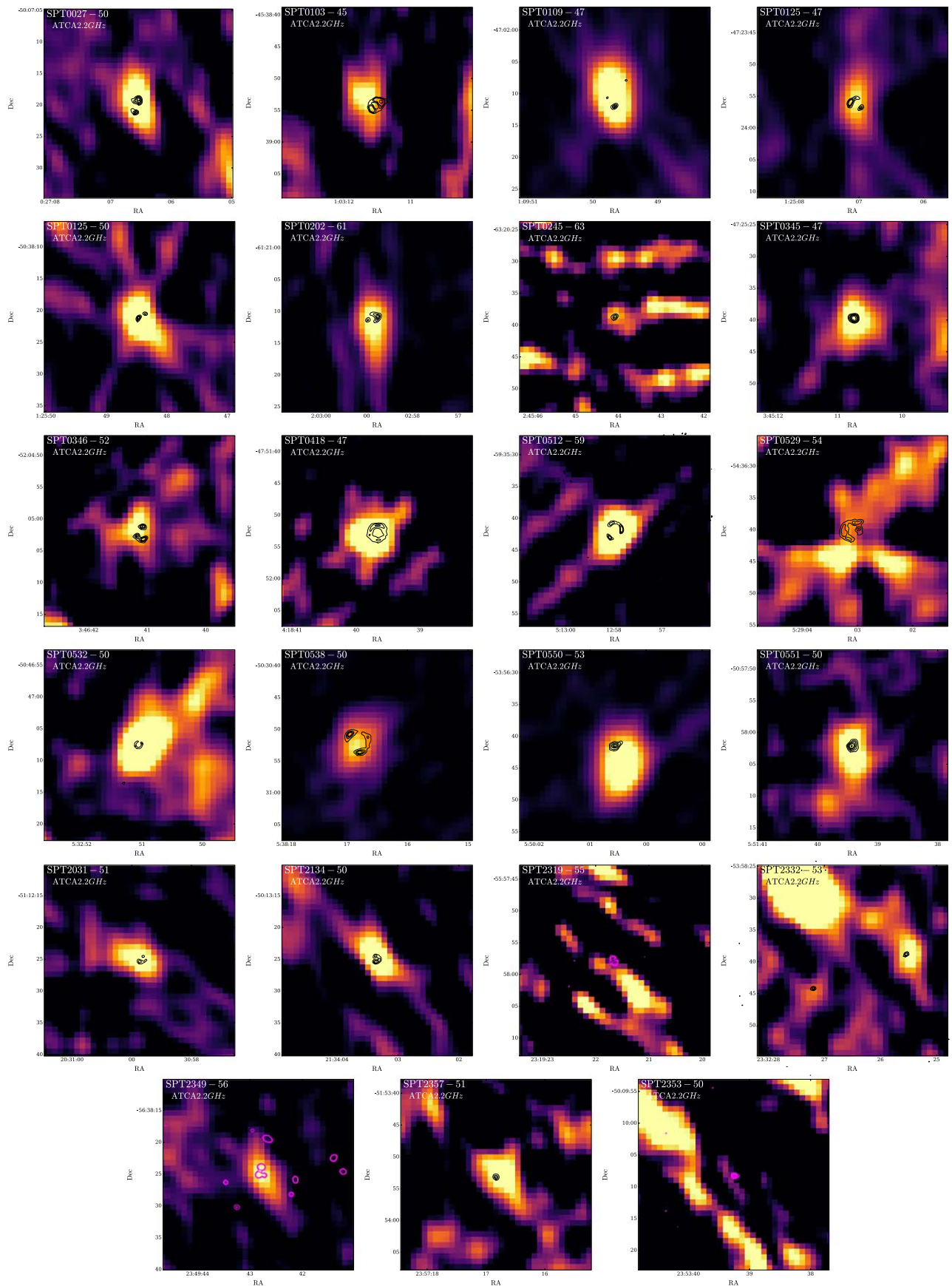


Figure 12. ATCA 2.2 GHz images ($30'' \times 30''$) of the 23 SPT-SMGs observed, with ALMA 850 μm contours overlaid (black, or alternatively pink when required for contrast).

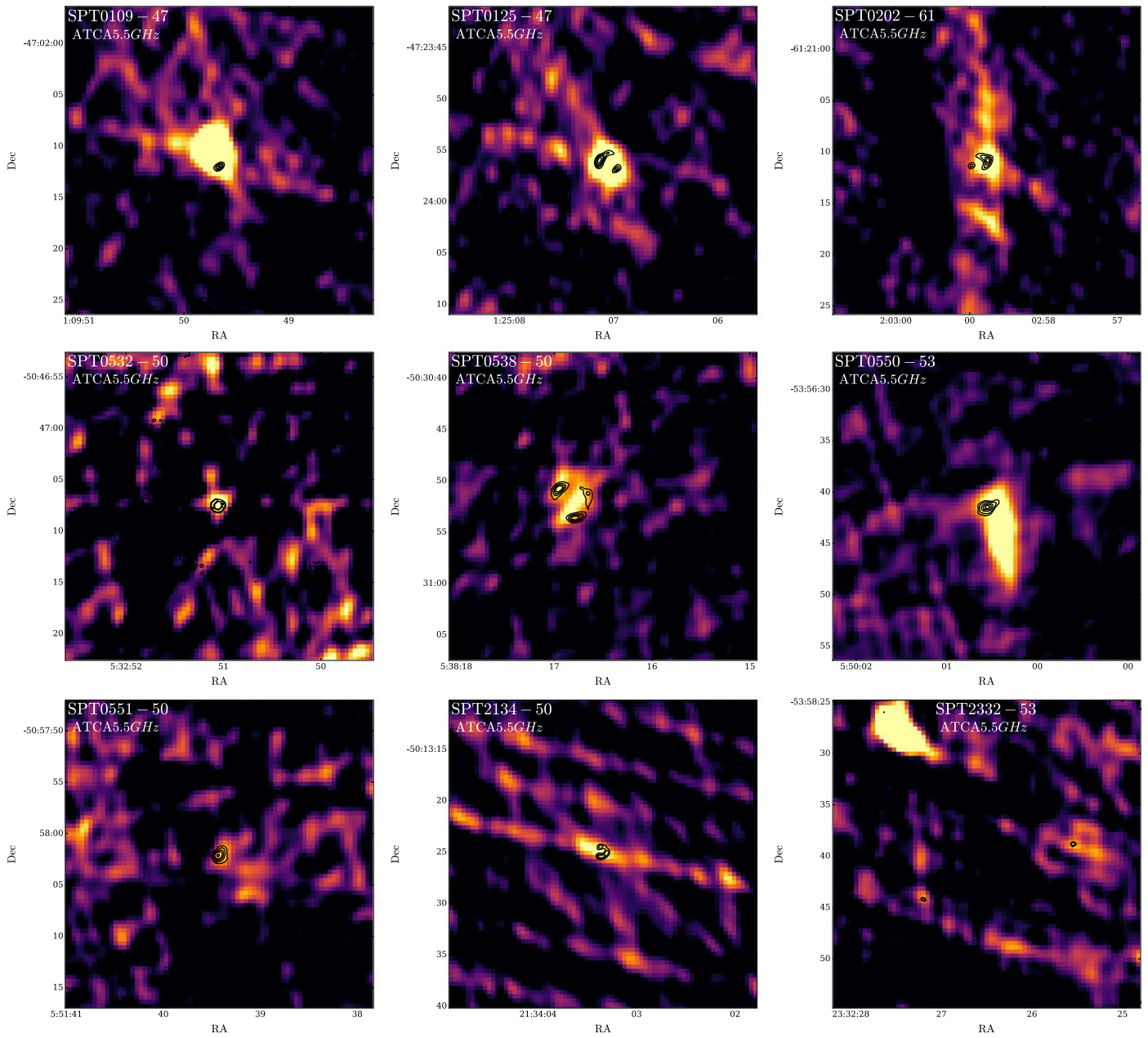


Figure 13. ATCA 5.5 GHz images ($30'' \times 30''$) of the nine detected SPT-SMGs, with ALMA $850 \mu\text{m}$ contours overlaid.

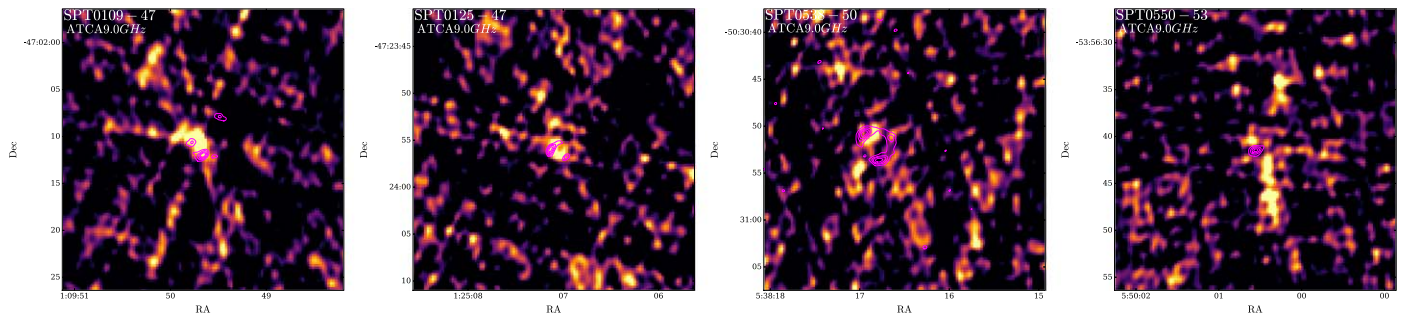


Figure 14. ATCA 9.0 GHz images ($30'' \times 30''$) of the four detected SPT-SMGs, with ALMA $850 \mu\text{m}$ contours overlaid.

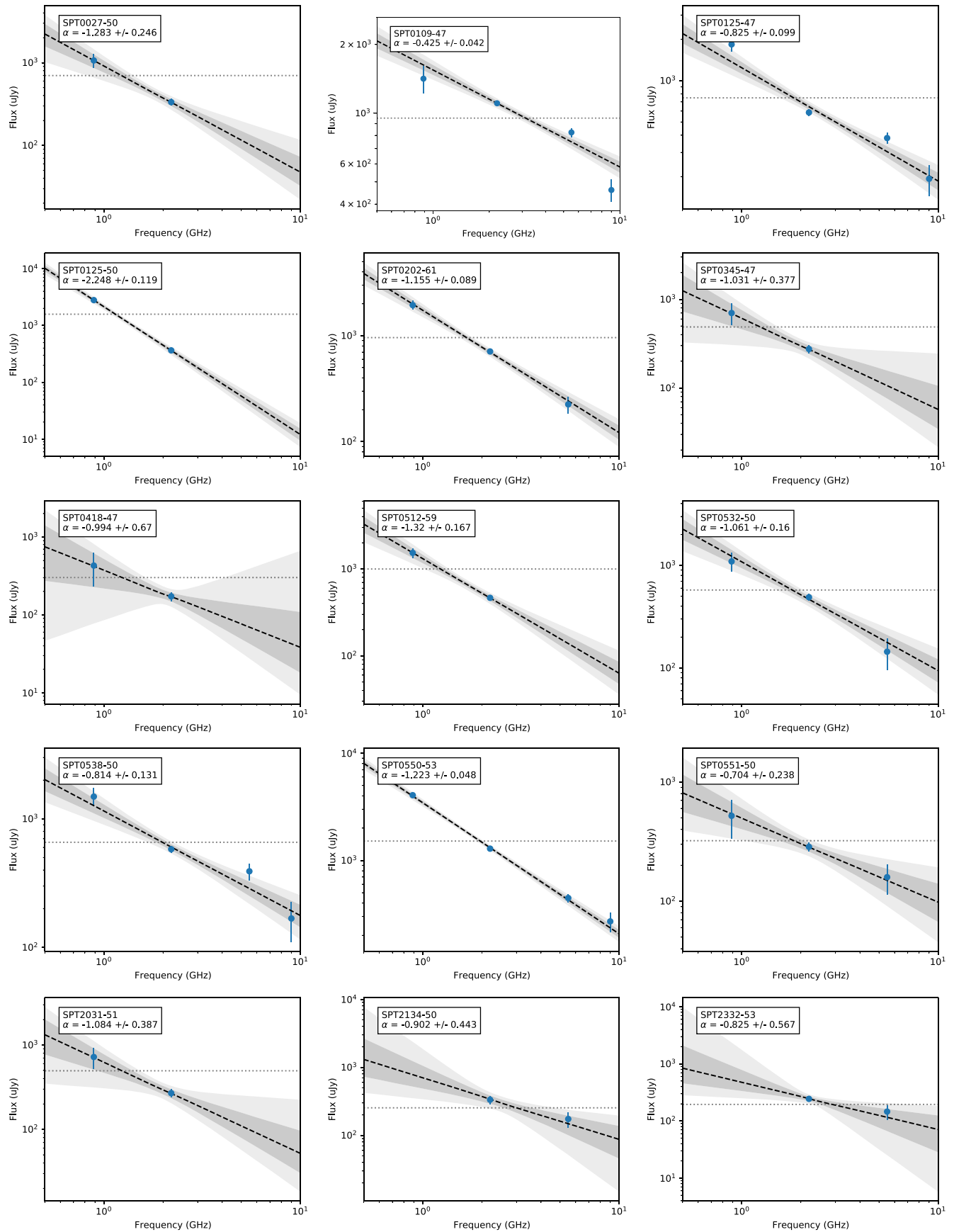


Figure 15. Radio spectral indices with errors constrained by MCMC modeling for gravitationally lensed SPT-SMGs having at least two detections between the ATCA and ASKAP follow-up. Gray shaded regions show the 1 and 2 σ uncertainties on α derived from the ATCA data. The brighter sources with steeper spectra are generally detected by the ASKAP RACS survey. The fit for SPT2349–56 is shown in Figure 2.

ORCID iDs

Scott C. Chapman  <https://orcid.org/0000-0002-8487-3153>
 Manuel Aravena  <https://orcid.org/0000-0002-6290-3198>
 Melanie Archipley  <https://orcid.org/0000-0002-0517-9842>
 Anthony H. Gonzalez  <https://orcid.org/0000-0002-0933-8601>
 Christopher C. Hayward  <https://orcid.org/0000-0003-4073-3236>
 Matt Malkan  <https://orcid.org/0000-0001-6919-1237>
 Dan P. Marrone  <https://orcid.org/0000-0002-2367-1080>
 Eric Murphy  <https://orcid.org/0000-0001-7089-7325>
 Emily Pass  <https://orcid.org/0000-0002-1533-9029>
 Kedar A. Phadke  <https://orcid.org/0000-0001-7946-557X>
 Cassie Reuter  <https://orcid.org/0000-0001-7477-1586>
 Kaja M. Rotermund  <https://orcid.org/0000-0002-9181-9948>
 Douglas Scott  <https://orcid.org/0000-0002-6878-9840>
 Manuel Solimano  <https://orcid.org/0000-0001-6629-0379>
 Justin Spilker  <https://orcid.org/0000-0003-3256-5615>
 Anthony A. Stark  <https://orcid.org/0000-0002-2718-9996>
 Nikolaus Sulzenauer  <https://orcid.org/0000-0002-3187-1648>
 Nick Tothill  <https://orcid.org/0000-0002-9931-5162>
 Joaquin D. Vieira  <https://orcid.org/0000-0001-7192-3871>
 David Vizgan  <https://orcid.org/0000-0001-7610-5544>
 Axel Weiss  <https://orcid.org/0000-0003-4678-3939>

References

- Apostolovski, Y., Aravena, M., Anguita, T., et al. 2023, arXiv:2301.01328
 Babul, A., Sharma, P., & Reynolds, C. S. 2013, *ApJ*, 768, 11
 Ballo, L., Heras, F. J. H., Barcons, X., & Carrera, F. J. 2012, *A&A*, 545, A66
 Banerji, M., Chapman, S. C., Smail, I., et al. 2011, *MNRAS*, 418, 1071
 Barger, A. J., Cowie, L. L., Chen, C. C., et al. 2014, *ApJ*, 784, 9
 Barger, A. J., Cowie, L. L., Owen, F. N., Hsu, L. Y., & Wang, W. H. 2017, *ApJ*, 835, 95
 Barger, A. J., Cowie, L. L., & Wang, W. H. 2007, *ApJ*, 654, 764
 Best, P. N., & Heckman, T. M. 2012, *MNRAS*, 421, 1569
 Birzan, L., Rafferty, D. A., McNamara, B. R., Wise, M. W., & Nulsen, P. E. J. 2004, *ApJ*, 607, 800
 Blain, A. W., Chapman, S. C., Smail, I., & Ivison, R. 2004, *ApJ*, 611, 725
 Blundell, K. M., & Kuncic, Z. 2007, *ApJL*, 668, L103
 Bothwell, M. S., Smail, I., Chapman, S. C., et al. 2013, *MNRAS*, 429, 3047
 Brienza, M., Godfrey, L., Morganti, R., et al. 2017, *A&A*, 606, A98
 Broderick, J. W., Bryant, J. J., Hunstead, R. W., Sadler, E. M., & Murphy, T. 2007, *MNRAS*, 381, 341
 Brodwin, M., Stanford, S. A., Gonzalez, A. H., et al. 2013, *ApJ*, 779, 138
 Carilli, C. L., & Walter, F. 2013, *ARA&A*, 51, 105
 Casey, C. M., Cooray, A., Capak, P., et al. 2015, *ApJL*, 808, L33
 Cavagnolo, K. W., McNamara, B. R., Nulsen, P. E. J., et al. 2010, *ApJ*, 720, 1066
 Chapman, S. C., Blain, A., Ibata, R., et al. 2009, *ApJ*, 691, 560
 Chapman, S. C., Blain, A. W., Ivison, R. J., & Smail, I. R. 2003, *Natur*, 422, 695
 Chapman, S. C., Blain, A. W., Smail, I., & Ivison, R. J. 2005, *ApJ*, 622, 772
 Chapman, S. C., Smail, I., Blain, A. W., & Ivison, R. J. 2004, *ApJ*, 614, 671
 Chen, C.-C., Smail, I., Ivison, R. J., et al. 2016, *ApJ*, 820, 82
 Chiaberge, M., Gilli, R., Lotz, J. M., & Norman, C. 2015, *ApJ*, 806, 147
 Chiang, Y.-K., Overzier, R., & Gebhardt, K. 2013, *ApJ*, 779, 127
 Cielo, S., Babul, A., Antonuccio-Delogu, V., Silk, J., & Volonteri, M. 2018, *A&A*, 617, A58
 Condon, J. J. 1997, *PASP*, 109, 166
 Connor, T., Donahue, M., Sun, M., et al. 2014, *ApJ*, 794, 48
 Daddi, E., Dannerbauer, H., Stern, D., et al. 2009, *ApJ*, 694, 1517
 Danielson, A. L. R., Swinbank, A. M., Smail, I., et al. 2017, *ApJ*, 840, 78
 Dannerbauer, H., Kurk, J. D., De Breuck, C., et al. 2014, *A&A*, 570, A55
 De Breuck, C., van Breugel, W., Minniti, D., et al. 1999, *A&A*, 352, L51
 De Breuck, C., van Breugel, W., Röttgering, H. J. A., & Miley, G. 2000, *A&AS*, 143, 303
 Dekel, A., Birnboim, Y., Engel, G., et al. 2009, *Natur*, 457, 451
 Di Matteo, P., Combes, F., Melchior, A. L., & Semelin, B. 2007, *A&A*, 468, 61
 Digby-North, J. A., Nandra, K., Laird, E. S., et al. 2010, *MNRAS*, 407, 846
 Ding, X., Silverman, J., Treu, T., et al. 2020, *ApJ*, 888, 37
 Dudzevičiūtė, U., Smail, I., Swinbank, A. M., et al. 2020, *MNRAS*, 494, 3828
 Ehlert, S., von der Linden, A., Allen, S. W., et al. 2014, *MNRAS*, 437, 1942
 Elbaz, D., Daddi, E., Le Borgne, D., et al. 2007, *A&A*, 468, 33
 Everett, W. B., Zhang, L., Crawford, T. M., et al. 2020, *ApJ*, 900, 55
 Fabian, A. C. 2012, *ARA&A*, 50, 455
 Foreman-Mackey, D., Conley, A., Meierjürgen Farr, W., et al. 2013, emcee: The MCMC Hammer, Astrophysics Source Code Library, ascl:1303.002
 Förster Schreiber, N. M., Genzel, R., Newman, S. F., et al. 2014, *ApJ*, 787, 38
 Geach, J. E., Alexander, D. M., Lehmer, B. D., et al. 2009, *ApJ*, 700, 1
 Gilli, R., Mignoli, M., Peca, A., et al. 2019, *A&A*, 632, A26
 Giodini, S., Smolčić, V., Finoguenov, A., et al. 2010, *ApJ*, 714, 218
 Gobat, R., Daddi, E., Onodera, M., et al. 2011, *A&A*, 526, A133
 Gómez-Guijarro, C., Riechers, D. A., Pavesi, R., et al. 2019, *ApJ*, 872, 117
 Guidetti, D., Bondi, M., Prandoni, I., et al. 2017, *MNRAS*, 471, 210
 Güsten, R., Nyman, L. A., Schilke, P., et al. 2006, *A&A*, 454, L13
 Haiman, Z., Spaans, M., & Quataert, E. 2000, *ApJL*, 537, L5
 Hardcastle, M. J., Evans, D. A., & Croston, J. H. 2007, *MNRAS*, 376, 1849
 Hardcastle, M. J., Williams, W. L., Best, P. N., et al. 2019, *A&A*, 622, A12
 Hatch, N. A., Overzier, R. A., Kurk, J. D., et al. 2009, *MNRAS*, 395, 114
 Helou, G., Soifer, B. T., & Rowan-Robinson, M. 1985, *ApJL*, 298, L7
 Heywood, I. 2020, oxkat: Semi-automated Imaging of MeerKAT Observations, Astrophysics Source Code Library, ascl:2009.003
 Heywood, I., Jarvis, M. J., Hale, C. L., et al. 2022, *MNRAS*, 509, 2150
 Hill, R., Chapman, S., Phadke, K. A., et al. 2022, *MNRAS*, 512, 4352
 Hill, R., Chapman, S., Scott, D., et al. 2020, *MNRAS*, 495, 3124
 Hill, R., Chapman, S. C., Scott, D., et al. 2019, *MNRAS*, 485, 753
 Hopkins, P. F., Kereš, D., Murray, N., Quataert, E., & Hernquist, L. 2012, *MNRAS*, 427, 968
 Hotan, A. W., Bunton, J. D., Harvey-Smith, L., et al. 2014, *PASA*, 31, e041
 Ibar, E., Ivison, R. J., Best, P. N., et al. 2010, *MNRAS*, 401, L53
 Ivison, R. J., Magnelli, B., Ibar, E., et al. 2010, *A&A*, 518, L31
 Jarugula, S., Vieira, J. D., Weiss, A., et al. 2021, *ApJ*, 921, 97
 Jonas, J. & MeerKAT Team 2016, The MeerKAT Radio Telescope, in Proceedings of MeerKAT Science: On the Pathway to the SKA (Trieste: SISSA)
 Kamenitzky, J., Glenn, J., Rangwala, N., et al. 2012, *ApJ*, 753, 70
 Kauffmann, G., White, S. D. M., Heckman, T. M., et al. 2004, *MNRAS*, 353, 713
 Kellermann, K. I., Pauliny-Toth, I. I. K., & Williams, P. J. S. 1969, *ApJ*, 157, 1
 Kenyon, J. S., Smirnov, O. M., Grobler, T. L., & Perkins, S. J. 2018, *MNRAS*, 478, 2399
 Kormendy, J., & Ho, L. C. 2013, *ARA&A*, 51, 511
 Krolik, J. H., & Chen, W. 1991, *AJ*, 102, 1659
 Lacaille, K. M., Chapman, S. C., Smail, I., et al. 2019, *MNRAS*, 488, 1790
 Lacy, M., Miley, G., Rawlings, S., et al. 1994, *MNRAS*, 271, 504
 Lagos, C. D. P., Bayet, E., Baugh, C. M., et al. 2012, *MNRAS*, 426, 2142
 Large, M. I., Mills, B. Y., Little, A. G., Crawford, D. F., & Sutton, J. M. 1981, *MNRAS*, 194, 693
 Law, D. R., Steidel, C. C., Erb, D. K., et al. 2009, *ApJ*, 697, 2057
 Lehmer, B. D., Alexander, D. M., Chapman, S. C., et al. 2009, *MNRAS*, 400, 299
 Macciò, A. V., Dutton, A. A., van den Bosch, F. C., et al. 2007, *MNRAS*, 378, 55
 Mantz, A. B., Abdulla, Z., Allen, S. W., et al. 2018, *A&A*, 620, A2
 Martini, P., Kelson, D. D., Kim, E., Mulchaey, J. S., & Athey, A. A. 2006, *ApJ*, 644, 116
 Matsuda, Y., Nakamura, Y., Morimoto, N., et al. 2009, *MNRAS*, 400, L66
 McConnell, D., Allison, J. R., Bannister, K., et al. 2016, *PASA*, 33, e042
 McConnell, D., Hale, C. L., Lenc, E., et al. 2020, *PASA*, 37, e048
 McMullin, J. P., Waters, B., Schiebel, D., Young, W., & Golap, K. 2007, in ASP Conf. Ser. 376, Astronomical Data Analysis Software and Systems XVI, ed. R. A. Shaw, F. Hill, & D. J. Bell (San Francisco, CA: ASP), 127
 McNamara, B. R., & Nulsen, P. E. J. 2012, *NJPh*, 14, 055023
 Mihoš, J. C., & Hernquist, L. 1994, *ApJL*, 431, L9
 Mihoš, J. C., & Hernquist, L. 1996, *ApJ*, 464, 641
 Miller, T. B., Chapman, S. C., Aravena, M., et al. 2018, *Natur*, 556, 469
 Miller, T. B., Hayward, C. C., Chapman, S. C., & Behroozi, P. S. 2015, *MNRAS*, 452, 878
 Muldrew, S. I., Hatch, N. A., & Cooke, E. A. 2015, *MNRAS*, 452, 2528
 Narayanan, D., Li, Y., Cox, T. J., et al. 2008, *ApJS*, 174, 13
 Newman, S. F., Shapiro Griffin, K., Genzel, R., et al. 2012, *ApJ*, 752, 111
 Nusser, A., Silk, J., & Babul, A. 2006, *MNRAS*, 373, 739

- Offringa, A. R., McKinley, B., Hurley-Walker, N., et al. 2014, *MNRAS*, **444**, 606
- Omont, A., Yang, C., Cox, P., et al. 2013, *A&A*, **551**, A115
- O’Sullivan, E., Giacintucci, S., David, L. P., et al. 2011, *ApJ*, **735**, 11
- Oteo, I., Ivison, R. J., Dunne, L., et al. 2018, *ApJ*, **856**, 72
- Overzier, R. A. 2016, *A&AR*, **24**, 14
- Overzier, R. A., Nesvadba, N. P. H., Dijkstra, M., et al. 2013, *ApJ*, **771**, 89
- Padovani, P. 2017, *FrASS*, **4**, 35
- Panessa, F., Tarchi, A., Castangia, P., et al. 2015, *MNRAS*, **447**, 1289
- Papadopoulos, P. P., van der Werf, P. P., Xilouris, E. M., et al. 2012, *MNRAS*, **426**, 2601
- Pentericci, L., Kurk, J. D., Carilli, C. L., et al. 2002, *A&A*, **396**, 109
- Radcliffe, J. F., Barthel, P. D., Garrett, M. A., et al. 2021, *A&A*, **649**, L9
- Ramos Almeida, C., Bessiere, P. S., Tadhunter, C. N., et al. 2012, *MNRAS*, **419**, 687
- Rasmussen, J., Mulchaey, J. S., Bai, L., et al. 2012, *ApJ*, **757**, 122
- Rennehan, D., Babul, A., Hayward, C. C., et al. 2020, *MNRAS*, **493**, 4607
- Renzini, A., & Andreon, S. 2014, *MNRAS*, **444**, 3581
- Reuter, C., Vieira, J. D., Spilker, J. S., et al. 2020, *ApJ*, **902**, 78
- Richards, G. T., Lacy, M., Storrie-Lombardi, L. J., et al. 2006, *ApJS*, **166**, 470
- Rotermund, K. M. 2020, PhD thesis, Dalhousie University hdl.handle.net/10222/78524
- Rotermund, K. M., Chapman, S. C., Phadke, K. A., et al. 2021, *MNRAS*, **502**, 1797
- Runco, J. N., Malkan, M. A., Fernández-Ontiveros, J. A., Spinoglio, L., & Pereira-Santaella, M. 2020, *ApJ*, **905**, 57
- Salomé, P., Guélin, M., Downes, D., et al. 2012, *A&A*, **545**, A57
- Seymour, N., Altieri, B., De Breuck, C., et al. 2012, *ApJ*, **755**, 146
- Simpson, J. M., Swinbank, A. M., Smail, I., et al. 2014, *ApJ*, **788**, 125
- Siringo, G., Kreysa, E., Kovács, A., et al. 2009, *A&A*, **497**, 945
- Smail, I., Chapman, S. C., Blain, A. W., & Ivison, R. J. 2004, *ApJ*, **616**, 71
- Spilker, J. S., Marrone, D. P., Aravena, M., et al. 2016, *ApJ*, **826**, 112
- Stacey, G. J., Hailey-Dunsheath, S., Ferkinhoff, C., et al. 2010, *ApJ*, **724**, 957
- Strandet, M. L., Weiss, A., Vieira, J. D., et al. 2016, *ApJ*, **822**, 80
- Taniguchi, Y., & Shioya, Y. 2000, *ApJL*, **532**, L13
- Thomson, A. P., Ivison, R. J., Simpson, J. M., et al. 2014, *MNRAS*, **442**, 577
- Tozzi, P., Gilli, R., Liu, A., et al. 2022a, *A&A*, **667**, A134
- Tozzi, P., Pentericci, L., Gilli, R., et al. 2022b, *A&A*, **662**, A54
- Travascio, A., Bongiorno, A., Tozzi, P., et al. 2020, *MNRAS*, **498**, 2719
- Trebtsch, M., Dubois, Y., Volonteri, M., et al. 2021, *A&A*, **653**, A154
- Umehata, H., Fumagalli, M., Smail, I., et al. 2019, *Sci*, **366**, 97
- van Breukelen, C., Simpson, C., Rawlings, S., et al. 2009, *MNRAS*, **395**, 11
- van der Werf, P. P., Isaak, K. G., Meijerink, R., et al. 2010, *A&A*, **518**, L42
- Venemans, B. P., Röttgering, H. J. A., Miley, G. K., et al. 2007, *A&A*, **461**, 823
- Vieira, J. D., Crawford, T. M., Switzer, E. R., et al. 2010, *ApJ*, **719**, 763
- Vito, F., Brandt, W. N., Lehmer, B. D., et al. 2020, *A&A*, **642**, A149
- Walter, F., Riechers, D., Cox, P., et al. 2009, *Natur*, **457**, 699
- Wang, G. C. P., Hill, R., Chapman, S. C., et al. 2021, *MNRAS*, **508**, 3754
- Wang, S. X., Brandt, W. N., Luo, B., et al. 2013, *ApJ*, **778**, 179
- Willott, C. J., Rawlings, S., Blundell, K. M., & Lacy, M. 1999, *MNRAS*, **309**, 1017
- Wootten, A., & Thompson, A. R. 2009, *Proc. IEEE*, **97**, 1463
- Wylezalek, D., Galametz, A., Stern, D., et al. 2013, *ApJ*, **769**, 79
- Yajima, H., Abe, M., Khochfar, S., et al. 2022, *MNRAS*, **509**, 4037
- Yang, H. Y. K., & Reynolds, C. S. 2016, *ApJ*, **829**, 90
- Yun, M. S., Hibbard, J. E., Condon, J. J., & Reddy, N. 1999, *Ap&SS*, **266**, 29